

Heinz Nixdorf-Lehrstuhl für Medizinische Elektronik
Prof. Dr. rer. nat. Bernhard Wolf
Technische Universität München



VALIDATION STUDY
OF A FINITE ELEMENT MODEL FOR REACTION
AND DIFFUSION USING ELECTRO-CHEMICAL AND
MATHEMATICAL METHODS
BACHELOR THESIS

BY

Safa MESSAOUD

RESIDENT IN:

Lerchenauer Str 41, App 29

80809 Munich

Tel: 01639842245

Supervisor Dr. rer. nat. Martin Brischwein
Dipl. –Ing. Daniel Grundl
Start date 07.03.2011
Completion date 22.06.2011

ACKNOWLEDGEMENT

I offer my regards and blessings to all those who supported me in any aspect during the completion of this thesis.

I am very grateful to Professor Dr. B. WOLF, Head of the Heinz Nixdorf Chair of Medical Electronics, for offering me the opportunity to work on this intriguing project and for always making sure that I have the most convenient conditions for the progress of my work.

I owe my deep gratitude to my supervisor Dr. Martin BRISCHWEIN, for the patient guidance, insightful comments and constructive criticisms he provided throughout my time as his student. I was fortunate to have a supervisor who gave me the freedom to explore on my own and at the same time the guidance to recover when my steps faltered.

I am very thankful to Mr. Daniel GRUNDL for the long discussions, the constructive criticism and advice during the preparation and correction of this thesis.

I would like to acknowledge Ms. Cornelia PFISTER, Mr. Franz DEMMEL and Mr. Thobias SCHWARZENBERGER for always being willing to help me.

Last but not least, none of this would have been possible without the love and patience of my family. My immediate family, to whom this thesis is dedicated to, has been a constant source of love, concern, support and strength.

INDEX

ACKNOWLEDGEMENT	2
INDEX	3
ABSTRACT	5
1 INTRODUCTION.....	6
2 METHODS AND EXPERIMENTAL.....	10
2.1 Software.....	10
2.2 Hardware	10
2.3 Geometry	12
2.4 Diffusion in liquid	14
2.5 The validation experiment: Anodic electrolysis of water.....	14
2.5.1 Experimental set up.....	14
2.5.2 The electrolysis flow	16
2.5.3 The Open Circuit Voltammetry	18
2.5.4 The Cyclic Voltammetry.....	18
2.6 Determination of the reaction rate	19
2.6.1 The protons' reaction rate	19
2.6.2 The oxygen's reaction rate.....	21
2.6.3 The electrolysis current.....	21
Kirchhoff's current law:	27
Kirchhoff's voltage law:	27
2.7 The buffer effects.....	30
2.7.1 Buffer effect on the reaction rate	32
2.7.2 Buffer effect on the diffusion coefficient.....	33
2.8 Implementation of the sensor response time	34
2.8.1 Operation mode of the opto chemical sensors	34
2.8.2 Modeling of the sensors	37
2.8.3 Determination of the sensor's impulse response	40
2.8.4 Implementation of the sensor response time in the diffusion-reaction model	43

3	RESULTS	45
3.1	Electrolysis results	45
3.2	COMSOL results	46
3.2.1	Simulation of the oxygen sensor readings	46
3.2.2	Simulation of the pH sensor readings	48
4	DISCUSSION.....	53
4.1	Model verification	53
4.2	Model validation.....	53
4.2.1	Comparison between the simulated and measured oxygen sensor kinetics.....	54
4.2.2	Comparison between the simulated and measured pH sensor kinetics.....	55
4.3	Sensitivity analysis:	57
4.4	Error analysis.....	58
4.4.1	Experimental errors.....	58
4.4.2	Geometry errors	65
4.4.3	Simulation errors.....	68
4.4.4	Quantitative error estimation	68
4.4.5	Summary of the error analysis	70
5	OUTLOOK.....	71
6	SUMMARY	74
7	LIST OF FIGURES	75
8	LIST OF TABLES	78
9	REFERENCES.....	79

ABSTRACT

Computational models are valuable tools for micro-metabolic studies on cellular specimens. For example, they can be used for the approximation of absolute cell metabolic rates (given in mol O₂/s or mol H⁺/s) from sensor kinetics measured on tumor tissue specimens explanted from cancer patients. The previously developed model calculates physico-chemical changes (pH value due to the extracellular acidification and dissolved oxygen concentrations due to the cellular oxygen uptake) of cell culture media in micro scaled volumes within so called “cell-on-a-chip-systems”. To make the simulated kinetics comparable to experimental kinetics, the sensor response time had to be included into the model. This was achieved by convolution of the sensor impulse response with the simulated sensor kinetics.

Like for every model, a careful validation has to show that it is a correct representation of the true experimental scenario under investigation. The goal of this study is to assess the validity of a 3D finite element model involving chemical reaction and diffusion. As a validation experiment, an electrochemical approach was chosen: By anodic electrolysis a chemical reaction has been actuated on an electrode structure to generate O₂ and H⁺ ions. Using Faraday's law, measurement of the electrolysis current gives the required reaction rate. Comparison of experimental sensor pH and O₂ sensor kinetics with the correspondent simulation kinetics yields the basis for model validation. In view of correlation coefficients ranging between 0.95 and 0.97 the outcome of the validation is positive. However, the validation process with its detailed error analysis also provided suggestions for a further improvement of measurement technology, namely the reduction of pH sensor response times and the increase of the sensor sampling rate.

1 INTRODUCTION

The development of microsystems or lab-on-a-chip devices for medical, biological and chemical applications is a rapidly growing field. Often, such devices include sensors, actuators and micro fluidic channels. The advantage of these micro-laboratories is that they enable massively parallel sample preparations, measurements as well as savings of costly drug compounds and valuable clinical samples.

The system treated in this work is a micro reaction chamber (MRC) from a multiwellplate, working with optochemical sensors for pH and dissolved oxygen. Cells or living tissues are cultured in the MRC. Their metabolic rates are monitored in real time with the mentioned sensors.

In order to identify possible artefacts, to improve the sensing geometry and to calculate absolute metabolic rates from sensor raw data, a three Dimensional Finite Element Model (FEM) of diffusion and chemical reaction in the MRC was set up.

Since the developed model is based on an idealized geometry and distinct assumptions for boundary conditions and chemical reactions, the verification of the mathematical and physical foundations as well as the validation of the results against experimental data are necessary. Verification is defined as ‘modeling the physical phenomena and solving the equations right’ and validation is ‘solving the right equations’. To investigate the robustness of the model, a sensitivity analysis is included. The sensitivity analysis is a technique for systematically changing the input parameters in a model to determine the effects of such changes on the output. Once this is achieved, the model presents a powerful tool for various applications. A valuable application of a validated diffusion and reaction model is the determination of absolute cell metabolic rates.

So far, such rates have been derived from the measured slopes of pH vs. time and dissolved oxygen vs. time by linear approximation. As outlined in this work, this implies a severe simplification. Moreover, only relative changes of such rates in the time course of an experiment can be quoted instead of absolute metabolic rates. The impact of a model is also evident, when new geometries of the MRC or sensor positions have to be tested or when the position of reacting sites (e.g. metabolically active cells or tissues) within the MRC is altered.

Actually, the validation could have been limited to the comparison of the simulation results with the experimental measurements from cell culturing, if all input parameters of the models

INTRODUCTION

were known. However, the cell reaction rates which may both depend on biological (biochemically regulated cell metabolic activity) and physical phenomena (physico-chemical parameters of the micro environment) are unknown and potentially variable in time. In order to have experimental control of all input parameters required for the model, we chose to use another approach for the validation. This approach involves the anodic electrolysis of water on electrode structures (interdigitated electrode structures, IDES) present next to the optochemical sensors for pH and dissolved oxygen. In fact, by applying a current density at the IDES at the bottom of the MRC, it is possible to produce dissolved oxygen and H^+ ions. The reaction rate is given by Faraday's law and defined by the measured current flow, as long as parasitic side reactions are excluded.

Within the framework of this thesis, the model of the involved reaction-diffusion processes was extended by implementation of the sensor characteristic impulse response. On basis of the extended model, it is possible to draw conclusions about the real pH values and oxygen concentrations from the measured sensor kinetics.

Fig 1.1 gives an overview of the model validation process.

INTRODUCTION

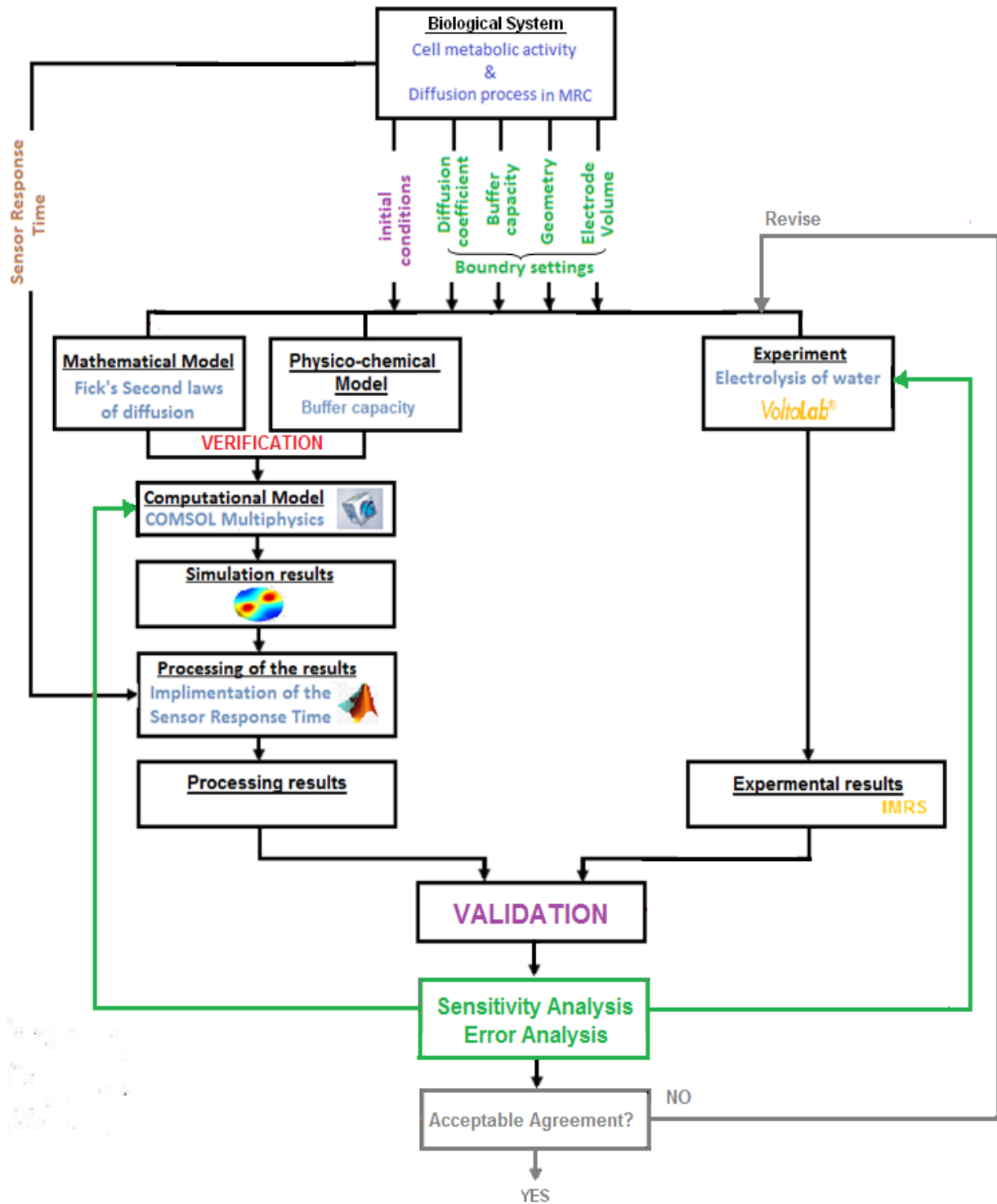


Fig 1.1: Flow of the verification and validation process. Validation is used to quantify the model's ability to describe the experimental outcomes of the physical system, given well defined boundary settings and initial conditions.

INTRODUCTION

The biological system to be modeled involves two cell metabolic processes: (1) the extrusion of acid (protons) and (2) the uptake of oxygen. Protons and dissolved oxygen diffuse in micro scaled reaction chambers integrating reacting sites (cell culture) as well as in the sensing sites.

The first step in the development of the model is the experimental determination of the input parameters, namely the boundary settings (definition of the initial conditions and geometry, measurement of the buffer capacity for pH modeling).

The second step is a mathematical and physico-chemical modeling of the reaction and diffusion processes in the MRC. In the case of the validation experiment, the reaction rate is defined by Faraday's law, which gives the stoichiometric relationship between electric charge and the amount of generated H^+ ions and oxygen. The diffusion process is mathematically described by the second order differential equation of the Fick's second law.

Once the input parameters are determined and the mathematical and physico-chemical models are set, COMSOL Multiphysics, a simulation program based on the finite element method, is used to approximate the sensor kinetics in the MRC, however, in the first instance, without consideration of the sensor response time. This model yields a spatio-temporal distribution of the expected pH and oxygen values.

The following step is the implementation of the sensor response time on the sensor kinetics. This was achieved with a MATLAB protocol after experimental determination of the actual response times.

The MATLAB-processed sensor kinetics are then compared with experimental kinetics obtained from the electrolysis experiments with concomitant sensing of pH and dissolved oxygen. If the model is an accurate representation of reality, a good agreement will be observed.

Next, a sensitivity analysis is carried out to test the robustness of the model by determination of the degree to which input parameters influence the output ones.

Finally, the degree of congruence has to be discussed on the basis of an error analysis.

The process is iterative until the model and validation experiments provide reasonable agreement within preset acceptance criteria.

2 METHODS AND EXPERIMENTAL

2.1 Software

- **COMSOL Multiphysics (3.5.a and 4.0):**

A finite element analysis, solver and simulation software package for various physics and engineering applications, especially coupled phenomena or “Multiphysics”.

The diffusion and reaction in the MRC are modeled with the “Chemical Reaction Engineering” module of the COMSOL software.

- **MATLAB:**

A numerical computing environment, used in this work to implement the sensor response time on the simulated sensor kinetics and to plot the pH and dissolved oxygen predicted curves.

- **Z view and Z plot Software:**

A control and data management system for measuring impedances, utilized in this thesis to determine the capacitive current’s parameters during the electrolysis.

2.2 Hardware

- **IMR System (Intelligent Micro Plate Reader):**

This was developed at the Heinz Nixdorf Chair for Medical Electronics at the Technical University of Munich. The IMR has been described in detail elsewhere [1]. It is a cell monitoring platform using automation-, sensor- and imaging technology. Cells are cultured and monitored in a sensor test plate (24 well). Fig. 2.1 is a photograph of the system.



Fig. 2.1: IMR system with embedded process microscope and pipetting robot in a cell culture incubator. The sensor test plate is in front position.

METHODS AND EXPERIMENTAL

The microscope can be replaced by a sensor readout box transmitting the excitation and emission light from the 24 oxygen- and 24 pH- sensors simultaneously. This readout box has been used for the experimental determination of sensor response times and for the electrolysis experiments.

Fig 2.2 shows the sensor test plate with sensors for pH, dissolved oxygen and electric impedance. Importantly, each cell culture is enclosed in a so called micro-reaction chamber (MRC). Tab 2.3 shows a schematic cross section of a single MRC.

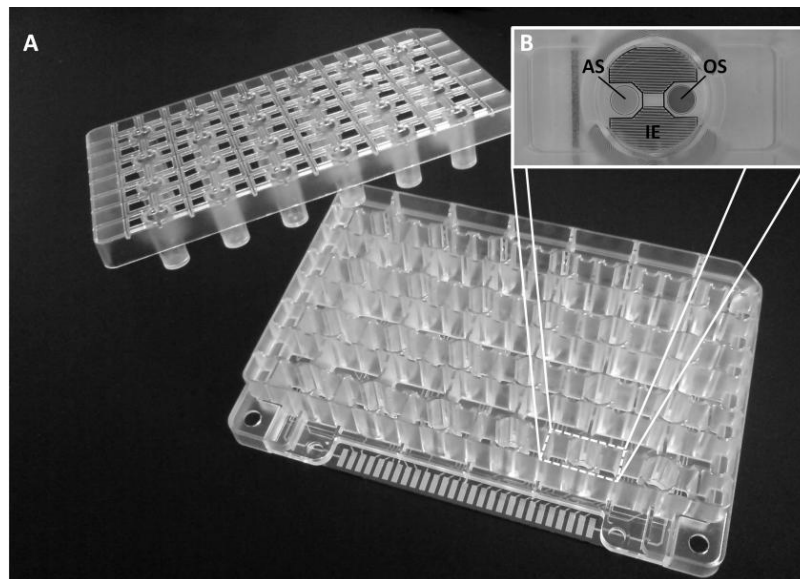


Fig 2.2: (A) The sensor test plate with its cover lid, confining 24 micro reaction volumes on each of the cell culture wells. The bottom of the plate is a glass substrate. (B) Enlargement of a single well in top view, with optochemical acidification sensor (AS), optochemical oxygen sensor (OS) and interdigitated electrode structure (IE).

For the experimental validation described in this work, the electrolysis was actuated with the interdigitated electrode structures shown in Fig 2.2 These are platinum thin film structures with a structure width and distance of 50 μm .

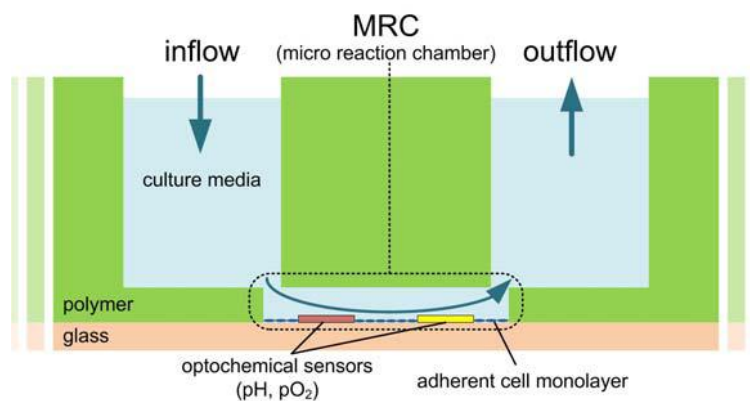


Fig 2.3: Pipetting system showing a MRC in cross section together with two hydrostatic side vessels

- **VoltaLab PGZ100:**

This is an electrochemistry work station with potentiostat and an impedance meter for electrochemical impedance spectroscopy (EIS).

A potentiostat is a device adjusting the desired potential at a working electrode versus a reference electrode. It does so by forcing a current to flow between the working electrode and a counter electrode while the reference electrode is left without current.

In this work, it was used for open circuit voltammetry, cyclic voltammetry and chronoamperometry.



Fig 2.4 : VoltaLab potentiostat

2.3 Geometry

The idealized geometry of a single MRC as a part of the multiwellplate is shown in Fig 2.5 (a). The MRC includes two optochemical sensor spots at the bottom. Each of the spotted sensors has a diameter of ≈ 2 mm with a height of ≈ 0.1 mm. The exact site, position and form of a sensor spot may differ from the ideal values. The MRC or well diameter is 7.7 mm. The height of the MRC (i.e the vertical distance between glass chip and the polymeric cover lid) is adjusted to ≈ 0.4 mm.

The resulting MRC volume and surface are respectively about 18 μL and 40 mm^2 .

In this work, the exact structure of the actuating electrodes was implemented in the model. Their form and dimension are presented in Fig 2.5. The resulting electrode surface is 27.6 mm². Fig 2.5 (c) and (d) show the resulting geometry in COMSOL representation.

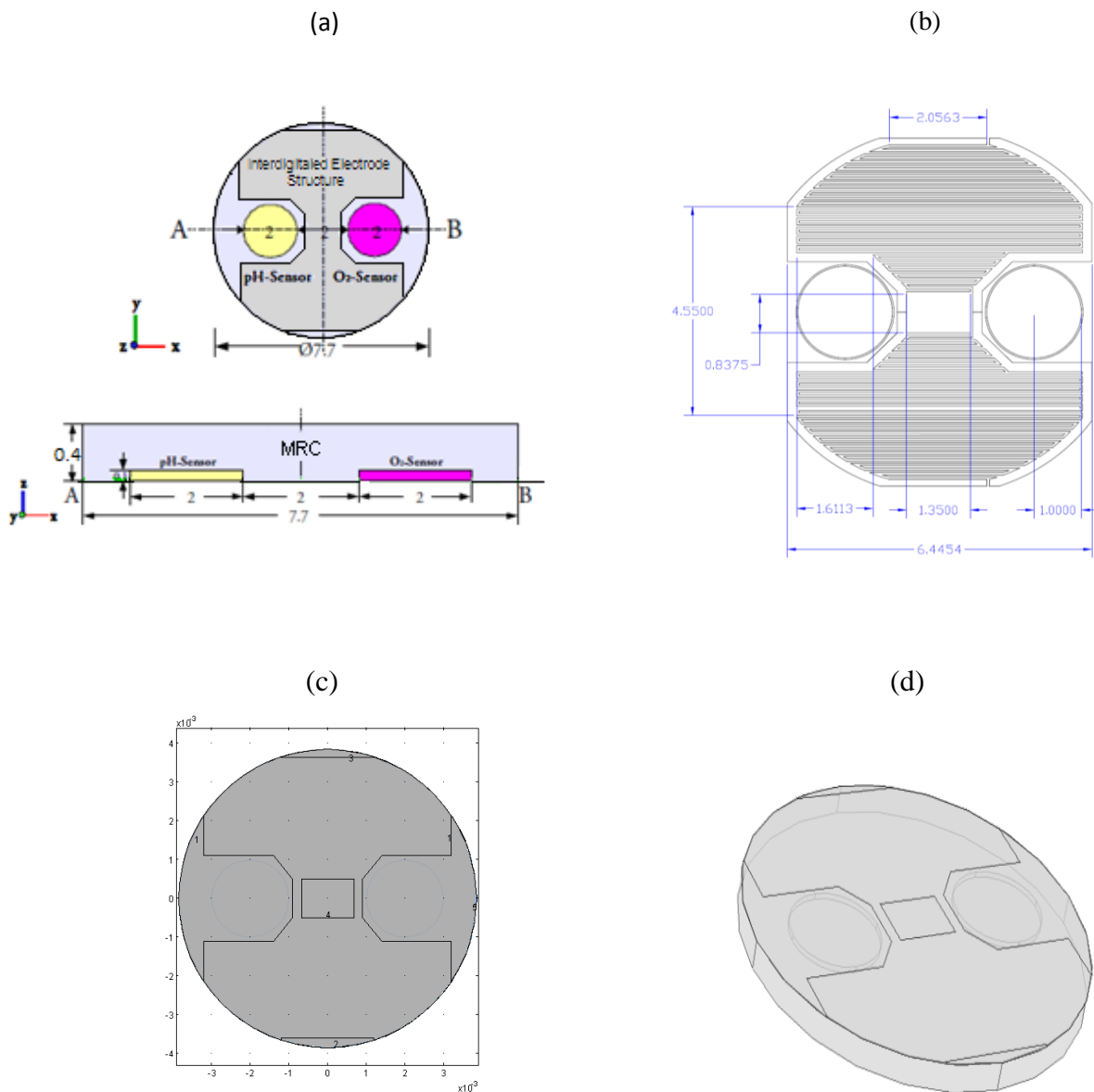


Fig 2.5: (a) Idealized Geometry of the MRC (at the top: top view, below: section), (b) Layout of the MRC with the electrode dimensions, (c) Two Dimensional geometry of the MRC in COMSOL representation, (d) Three Dimensional geometry of the MRC in COMSOL representation.

2.4 Diffusion in liquid

The mathematical formulation of the diffusion process is given by the Fick's second law, stating that the time dependant concentration and the mass transport of a substance in a static liquid depend on the gradient of the concentration. This relation is described by the diffusion equation:

$$\frac{\partial c}{\partial t} + \nabla \cdot (-D \nabla c) = R \quad (2.1)$$

Where:

- c The concentration of the protons or dissolved oxygen
- D The coefficient of diffusion.
- R The generation rate of the protons and oxygen molecules on the surface of the IDES (Interdigitated Electrode Structures)

Starting conditions are a pH value of 7.4 and a dissolved oxygen concentration of 0.214 mmol/L (physiologic salt solution saturated with dissolved O₂ under atmospheric conditions, i.e. pressure of 1013 hPa and 20.95% percent oxygen at 25°C).

2.5 The validation experiment: Anodic electrolysis of water

2.5.1 Experimental set up

The anodic electrolysis of water involves the decomposition of H₂O molecules at a redox electrode into oxygen molecules (O₂) and protons (H⁺) or, more exactly, hydronium ions (H₃O⁺ ions). This process occurs at appreciable rates on a platinum working electrode at voltages more positive than about 1 V (vs. a silver/silver chloride reference electrode, saturated KCl). The stoichiometrically correct redox reaction (assuming that a 4-electron mechanism is exclusively observed) is:



An important conceptual basis for the validation process is Faraday's law giving the proportionality between the amount of oxygen generated and the flowing charge measured with the amperometer:

$$\int I_{gen}(t) dt = z \cdot F \cdot \Delta n \quad (2.3)$$

Where:

I_{gen} the Faraday current generated during the electrolysis

F the Faraday constant (96,485 C mol⁻¹)

z the stoichiometric number of electrons transferred per mol of the produced substance

Δn the amount of substance (number of moles) produced

Theoretically, the anodic oxygen evolution may also imply a two-step mechanism involving the generation of peroxide as an intermediary product. If this product diffuses away from the electrode, a decreased oxygen generation efficacy in relation to the charge measured is engendered. However, the addition of the enzyme catalase converting H₂O₂ very rapidly into H₂O and O₂, did not cause any detectable increase of the observed oxygen generation. Thus, the assumption of a predominating 4-electron (one-step) oxidation mechanism appears to be justified.

The main components required to achieve electrolysis are the electrolyte, the electrodes and the electric power supply.

- **The electrolyte**

The electrolyte is a substance containing mobile ions which are the carriers of electric current in the electrolyte. For the validation experiment the electrolyte is a buffer solution with an initial pH value of 7.4, composed of:

- a) **0.1g/0.5L** of Potassium Diphosphate **KH₂PO₄** (the acid).
- b) **0.72 g/0.5L** of Sodium Hydrogen Phosphate **Na₂HPO₄** (the base)
- c) **5.86g/0.5L** of sodium nitrate NaNO₃ as a conducting salt

Sodium nitrate was chosen instead of sodium chloride to exclude the anodic generation of Cl₂ from chloride ions as a possible electrochemical side reaction. Such a side reaction would also disrupt the validity of Faraday's law. Nitrate ions are electrochemically inactive in the potential range considered.

The electrolysis experiment was carried out twice, each time by pipetting 500 μL of the prepared buffer solution in the MRC. In the second experiment, 0.44 g/80 ml egg albumin was added to the electrolyte in order to investigate the effect of large buffering species on proton diffusion. The amount of albumin added resulted in the same increase of the buffer capacity as in case of addition of 5% fetal calf serum. However, the addition of serum was avoided, again in order to exclude chloride ions from the electrolyte solution.

- **The electrodes**

The electrodes are electrical conductors which provides the physical interface between the electrical circuit and the electrolyte. In this work, the contact pads for the two fingers of the interdigitated electrode structures, used for the electrolysis experiment, were combined to give a single thin-film platinum working electrode.

A wire gold electrode was used as a common (quasi-) reference (RE) and counter electrode. This wire gold collects the current flowing at the working electrode (WE) and should have at least the same surface area as it. The (RE) is polarized cathodically by the potentiostat. The involved redox process (presumably the cathodic decomposition of water into H_2) is spatially separated from the WE environment to avoid electrochemical crossover.

2.5.2 The electrolysis flow

Generally, a DC supply needs to be connected to the electrode metal wires so that a suitable DC current flows. An electric field is accordingly set up in the solution between the electrodes. Positive ions (Na^+) migrate to the cathode (in the same direction as the E-field). Negative Ions (NO_3^- and PO_3^-) migrate into the opposite direction (the same direction as the electrons in the wires). This ion transport process is called the migration. Uncharged species are transported by diffusion along with a concentration gradient.

If the electrochemical double layer is sufficiently polarized, a charge transfer reaction happens at the electrodes. Both the migration and diffusion process are presented in Fig. 2.6.

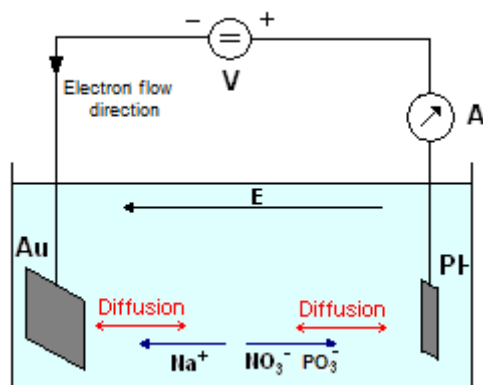


Fig. 2.6: Set up and flow of the electrolysis

Two different reactions happen at the cathode and anode:

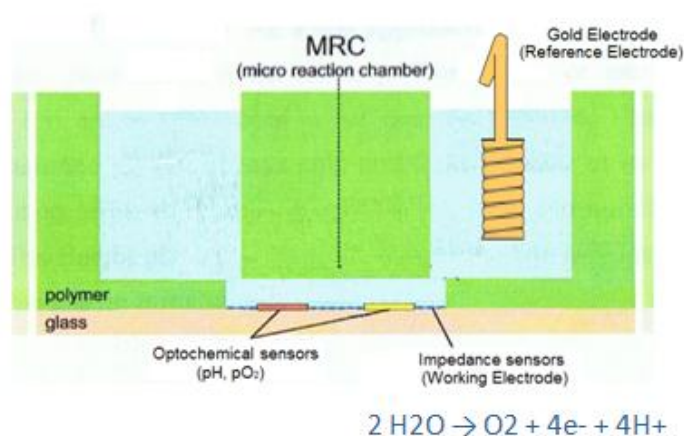
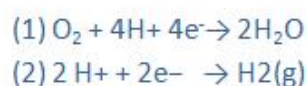


Fig 2.7: The reduction and oxidation reactions occurring during the electrolysis experiment

At the cathode

The discharge of sodium (Na^+) ions to metallic sodium requires extremely cathodic potentials. At much lower voltages, two other processes start: (1) the reduction of dissolved neutral oxygen and (2) the reduction of water to form H_2 .



Presumably, both reactions occur simultaneously at the common (quasi-) reference and counter electrode used for the electrolysis experiment.

At the anode

Both NO_3^- and PO_3^- need very large positive voltages to deliver their electrons to the anode. Chloride ions, however, could be discharged at the anode yielding chlorine gas (Cl_2) at lower voltages. From a thermodynamic point of view, the required voltage is similar to that which is needed for the anodic oxidation of water. Concentration and activation energies determine the relative rates of both processes. Since the water (the solvent in our case) is present in very large concentrations, this anodic reaction usually dominates. However, to preserve the validity of Faraday's law, each parasitic side reaction pathway should be excluded.

The voltage required for the anodic water oxidation reaction was determined with cyclic voltammetry (section 2.5.4). The water oxidation is given by the chemical equation (2.2).

2.5.3 The Open Circuit Voltammetry

The first step in the electrolysis experiment is the determination of the open circuit voltage (also referred to as the equilibrium potential or the rest potential) between the working electrode and the reference-/counter electrode. The open circuit potential was measured with the VoltaLab device. It corresponds to +240 mV (working electrode vs. reference-/counter electrode).

2.5.4 The Cyclic Voltammetry

An applied DC voltage does not necessarily lead to the current flow. A sufficiently high voltage must be applied to overcome the energy barrier at the electrode surfaces and the mass transport resistances. The required electrolysis potential was determined by means of cyclic voltammetry. In cyclic voltammetry, the electrode potential ramps linearly versus time as shown in Fig 2.8 (a). The potential is applied between the reference electrode and the working electrode. The current is measured between the working electrode and the counter electrode. This data is then plotted as current (I) vs. potential (V). As the waveform shows, the forward scan produces a current peak for the oxidation of H_2O . The current will increase as the potential reaches the oxidation potential of the analyte, but then falls off as the diffusional transport resistances (e.g. transport of the generated oxygen away from the electrode, transport of water molecules to the electrode) increase due to the concentration gradients decreasing with time.

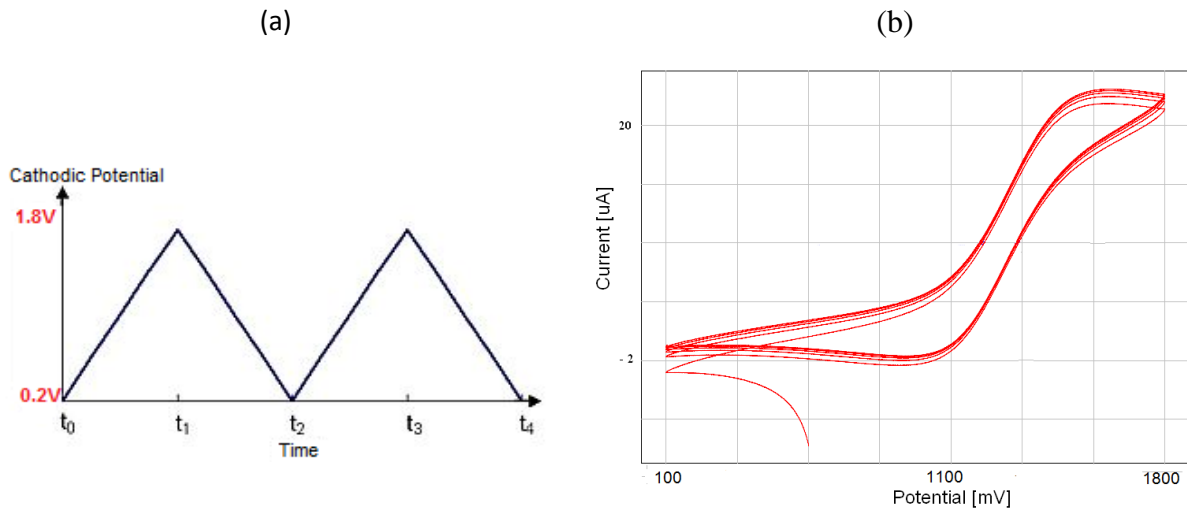


Fig 2.8: (a) Cyclic Voltammetry waveform (b) Typical cyclic voltammogram

As shown in the cyclic voltammogram, the required anodic potential should be at least ≈ 1.1 V. The potential should be as small as possible so that it remains below the onset of macroscopic gas bubble formation and other chemical reactions, but also large enough to detect the concentration changes of protons and oxygen with a sufficient resolution. The optimal design was determined empirically by varying the potential and comparing the measured curves with the simulated ones. A potential of 1200 mV fulfilled the requirements, although the detectable pH changes were relatively small. To obtain a better resolution of the pH decrease, a second electrolysis experiment with a working potential of 1500 mV was carried out. The results are presented in section 3.

2.6 Determination of the reaction rate

2.6.1 The protons' reaction rate

The reaction rate is the increase (also decrease) in molar concentration of a product of a reaction per unit time.

In this work it is defined by the current measured in the electrolysis through the volume of the electrodes. This assumption is justified by Faraday's law stating that the quantity of a substance produced by electrolysis is proportional to the quantity of electricity measured.

If one ampere electric current flows through a cross-sectional area in 1 Second, 1 Coulomb has passed. The Faraday constant F is the charge of 1 mol electrons.

METHODS AND EXPERIMENTAL

$$\begin{aligned} F &= \text{Avogadro's Number} \times \text{charge of one electron in coulombs} \\ &= 6.022 \times 10^{23} \text{ (mol}^{-1}\text{)} \times 1.602192 \times 10^{-19} \text{ (C)} \\ &= 96\,484 \text{ C mol}^{-1} \end{aligned} \quad (2.6)$$

This is usually rounded off to 96 500 C mol⁻¹ for calculations in chemistry.

To define the reaction rate, the stoichiometric relationship between protons produced and current flow must be known. This ratio is unity (see formula 2.2).

As a result the reaction rate is given by the formula:

$$R_{H^+}(t) = \frac{I(t)}{V \cdot F} \quad (2.7)$$

Where:

- R_{H^+} Reaction rate (mol s⁻¹·mm⁻³)
- I The Faraday current (A)
- F The Faraday constant (C mol⁻¹)
- V The volume of the electrodes (mm³)

In fact, the electrochemical reaction occurs exclusively at the electrode's surface giving rise to a flux of protons. In the solution, the current spreads out from the electrodes surface. A flux is defined as the flow rate through a cross-sectional area, so current density is a flux density.

The total sum of oxygen molecules passing through the electrodes is the current density, integrated over the whole cross sectional area and per second this must equal the electronic charge in the external electrode wire.

As a result the protons flux is given by the formula:

$$F_{H^+}(t) = \frac{I(t)}{A \cdot F} \quad (2.8)$$

Where:

- $F_{H^+}(t)$ Inward flux density (mol s⁻¹·mm⁻²)
- I(t) The Faraday current (A)
- A The surface of the electrodes (mm²)

2.6.2 The oxygen's reaction rate

Analog to the protons' reaction rate, the oxygen rate is:

$$R_{O_2}(t) = \frac{I(t)}{4 \cdot V \cdot F} \quad (2.9)$$

The multiplication with (1/4) is necessary because of the stoichiometric coefficients in the water dissociation equation (2.2): The dissociation of two water molecules results in the generation of four protons, four electrons and one oxygen molecule. If one mol of oxygen is generated, four moles of H⁺ ions should have been generated too. That means that the generation rate of the protons is four times higher than the one of the oxygen molecules.

The same applies to the flux density:

$$F_{O_2}(t) = \frac{I(t)}{4 \cdot A \cdot F} \quad (2.10)$$

2.6.3 The electrolysis current

The electrolysis current was determined by means of chronoamperometry. This electrochemical technique means an adjustment of a constant working potential and measuring of the current at the electrode. In our case, the voltage was set to +1200 mV or to +1500 mV (after a short interval at open circuit potential), as shown in Fig 2.9. The current has a sharp peak followed by a slow decay which can be approximately described by the Cottrell equation (see below) for Faraday currents. Prior to the start of the chronoamperometry, the pH and oxygen measurements with the IMR system were started to include a preelectrolysis interval with stable values.

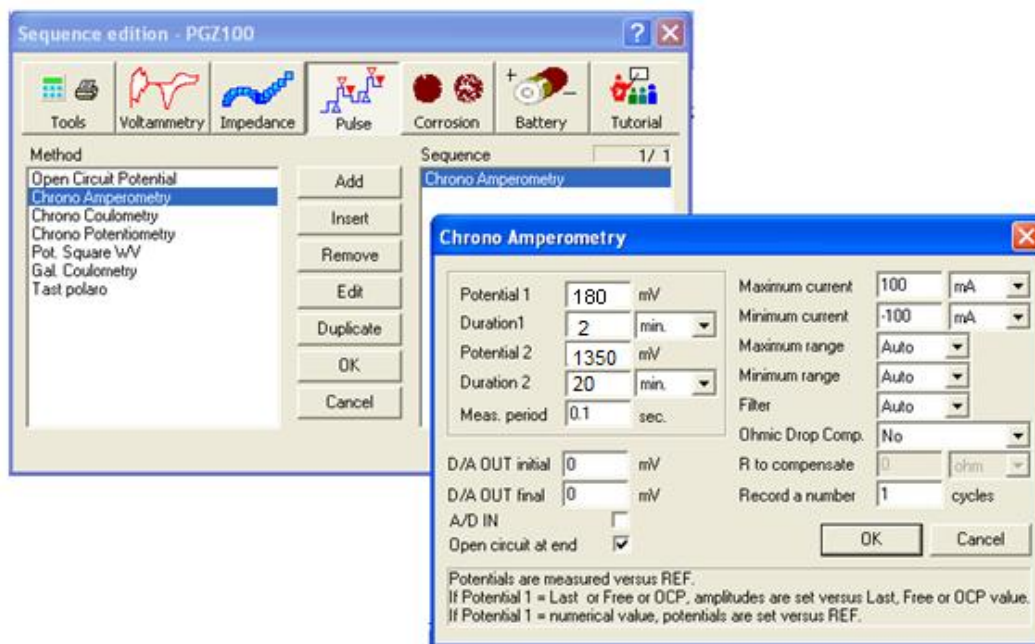


Fig 2.9: The Chronoamperometry set up with the VoltaLab

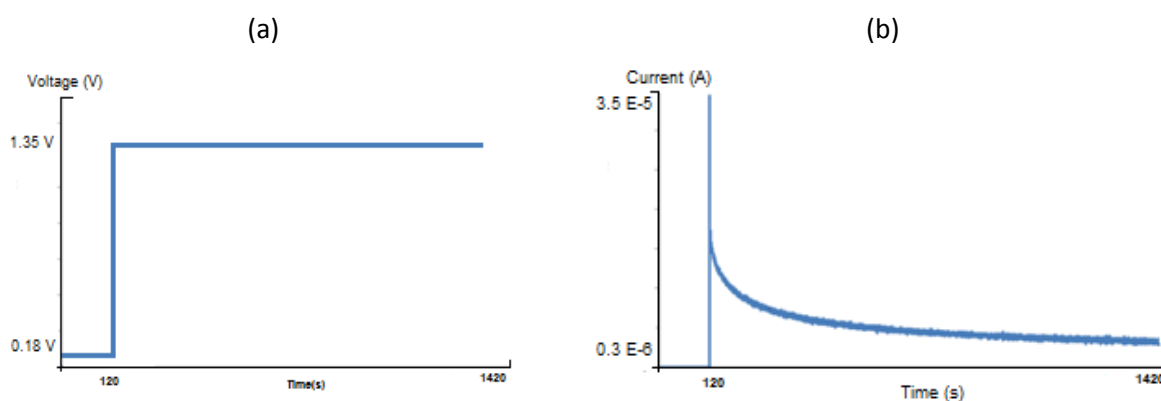


Fig 2.10: Chronoamperometry, (a) voltage vs. time, (b) current vs. time, measured for a redox potential of 1.2V

The current obtained from the electrolysis entails two components: (1) the current due to charging the electrode double-layer and (2) the Faraday current due to the electron transfer across the double layer, involving an electrochemical redox reaction.

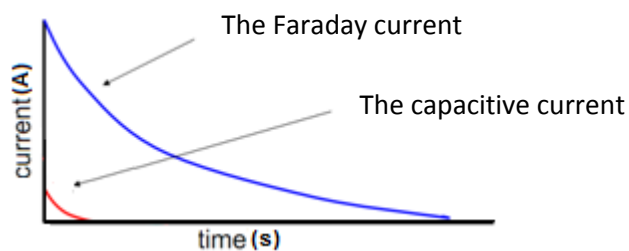


Fig 2.10: Components of the output signal in the chronoamperometry.

The capacitive current

The capacitive current is the current responsible for changing the potential of the working electrode from E_i (initial potential) to E_f (final potential) with respect to the reference electrode. It is instructive to model this situation as being analogous to charging a capacitor (Fig 2.11). In this circuit, a resistor, R_1 is placed in series with a capacitor C which is in parallel with a resistance R_2 . A switch SW , when closed, imposes V_b (the potential delivered by the VoltaLab).

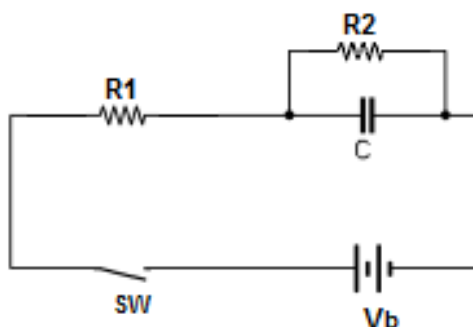


Fig 2.11: The electrode double layer's equivalent electrical circuit

The capacitance C [6]

At the electrode liquid interface the conversion from electronic to ionic conduction occurs.

In this transition zone, there will be a non uniform distribution of charges (Fig 2.12). According to the poisson equation, this results in an electrical potential across the interphase. This effect is particularly pronounced at the interphase between a solid and a polar medium which is water in our case. When the polar medium is liquid, the ion mobility is high; the formation of an electric double layer will take place in the liquid phase. The double layer can be thought as a molecular capacitor where one plate is represented by the charges in the metal, and the other plate by the polar water molecules at a minimum distance in the solution. The distance between the plates is of the order of 0.5 nm, so the capacitance values are enormous.

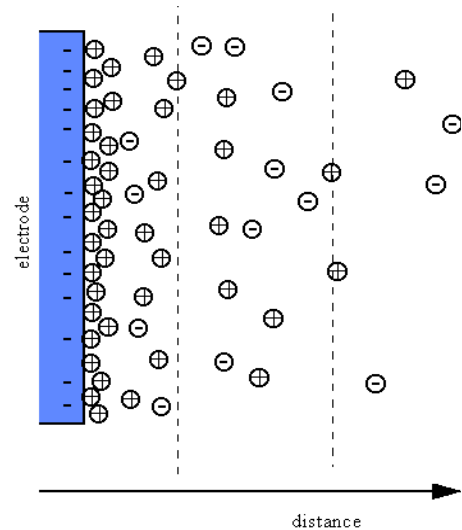


Fig 2.12: The distribution of ions at the metal/solution interface [6]

The Resistance R_1

The bulk of the electrolyte obey's the Ohm's law. Accordingly, the bulk electrolyte is modeled as an ideal resistor R_1 in serial with the electrode components. R_1 is frequency independent but depends on the geometry and the conductivity of the solution.

The Resistance R_2

R_2 is the faraday impedance. It represents the electron transfer across the interphase.

The values of R_1 , R_2 and C are approximated by the Electrochemical Impedance Spectrometry (EIS). For this purpose the "Z view" and "Z Plot" Software were used. By EIS, the impedance of a system over a range of frequencies is measured.

An AC Voltage of small amplitude (30 mV) and frequency f (ranging between 10^1 and 10^6 Hz) is applied between the working and reference electrodes in the electrolysis setup (Fig 2.13).

METHODS AND EXPERIMENTAL

Both the real Z_{Re} and imaginary part Z_{Im} of the Impedanz Z ($Z = dU_{WR}/dI = Z_{Re} + iZ_{Im}$) are obtained as a function of f . Upon cross plotting Z_{Im} against Z_{Re} , a Nyquist plot is obtained (Fig 2.14).

A charge transfer reaction appears ideally as a semi circle that is a combination of a resistor and capacitor connected in parallel.

The first intersect of the semi circle with the axis gives R_1 and the second intersect gives $R_1 + R_2$. The capacitance C can be computed from the frequency value f_m at the top of the semi circle ($C = 1/2\pi f_m R_2$).

These values are automatically given by the Z_Plot Software as shown in Fig 2.15.

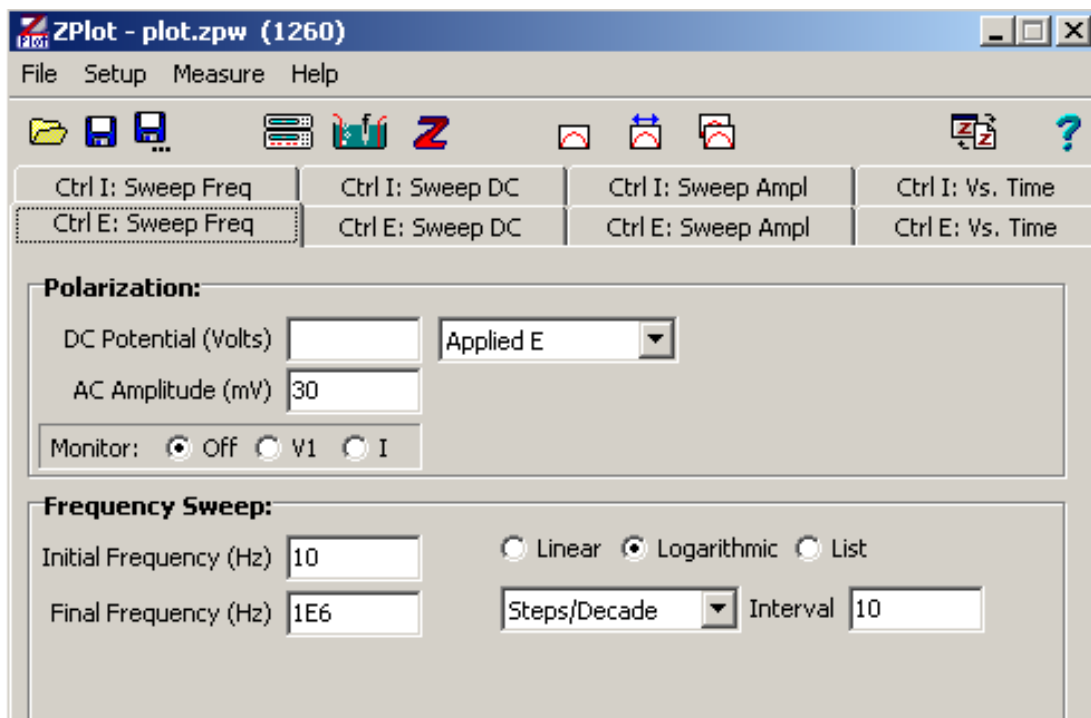


Fig 2.13: The Z Plot Software Interface showing the Impedance Spectroscopy parameters

METHODS AND EXPERIMENTAL

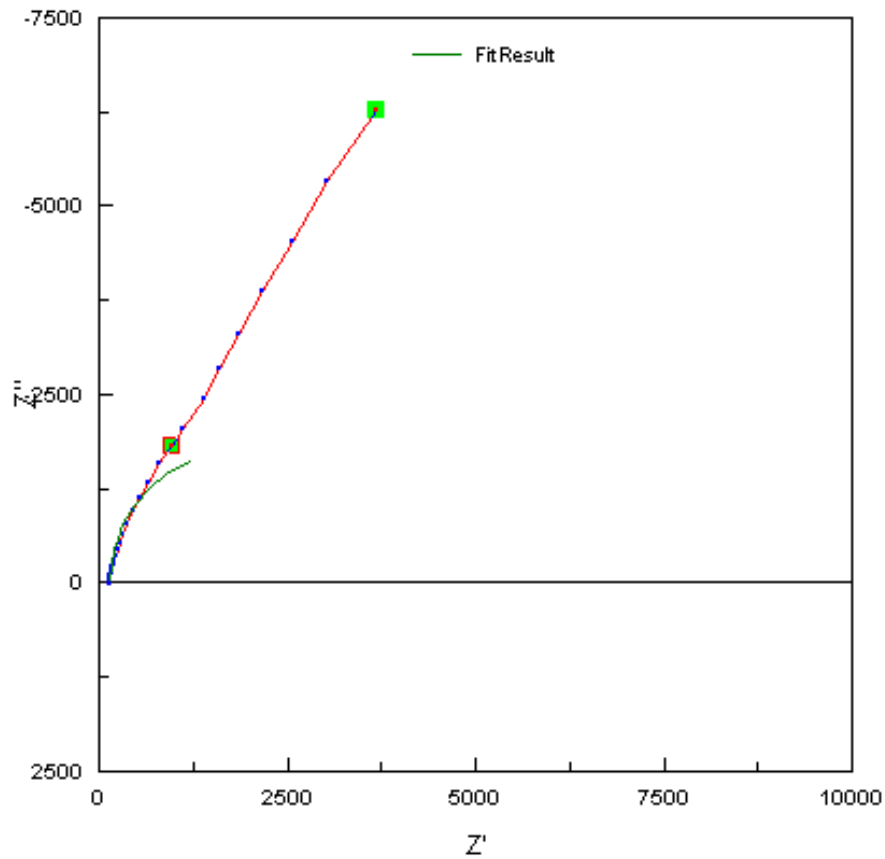


Fig 2.14: The Nyquist Plot of the MRC System circuit model. The red curve is the measured curve, the green one is the fitting curve.

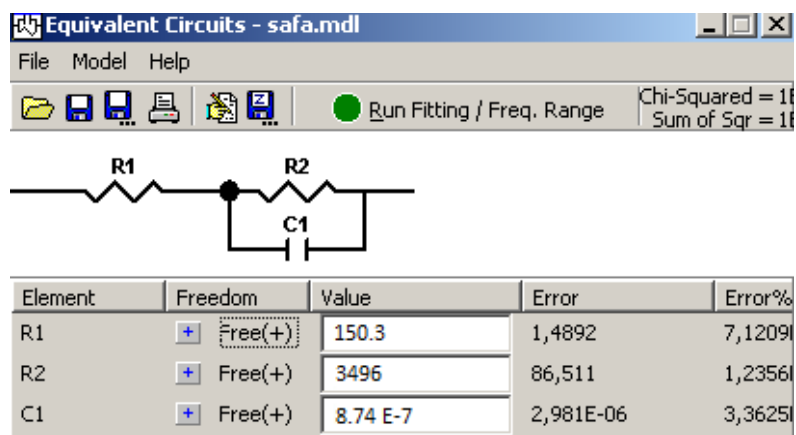


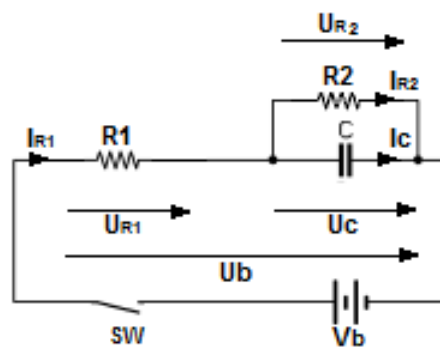
Fig 2.15: The equivalent circuit of the MRC given by the Z-Plot program

C, R₁ and R₂ values for both the solution with and without albumin are shown in Tab 2.1.

	Buffer solution without albumin	Buffer solution with albumin
R1	150.3 Ω	160 Ω
R2	3496 Ω	3931Ω
C	8.74 E-7	9.24E-7

Tab 2.1: The Impedance spectroscopy results

The circuit is analyzed to determine the capacitive current $i_c(t)$



Kirchhoff's current law:

$$i_{R_2}(t) + i_c(t) = i_{R_1}(t) \quad (2.11)$$

Kirchhoff's voltage law:

$$U_b = u_{R_1}(t) + u_c(t) \quad (2.12)$$

$$U_b = R_1 \cdot i_{R_1}(t) + u_c(t) \quad (2.13)$$

R₂ is parallel to C

$$u_{R_2}(t) = u_c(t) \quad (2.14)$$

The capacitance characteristic equation:

$$i_c(t) = C \cdot \frac{du_c(t)}{dt} \quad (2.15)$$

As result:

$$\frac{du_c(t)}{dt} = \frac{i_c(t)}{C} \quad (2.16)$$

(2.9) and (2.14) give

$$\frac{du_c(t)}{dt} = i_{R_1}(t) + i_{R_2}(t) \quad (2.17)$$

(2.11) and (2.15) give:

$$\frac{du_c(t)}{dt} = \frac{U_b}{R_1 \cdot C} - \frac{u_c(t)}{C} \left(\frac{1}{R_1} + \frac{1}{R_2} \right) \quad (2.18)$$

Because $R_1 \ll R_2$:

$$\frac{du_c(t)}{dt} = \frac{U_b}{R_1 \cdot C} - \frac{u_c(t)}{C} \left(\frac{1}{R_1} \right) \quad (2.19)$$

The solution of the previous equation is:

$$u_c(t) = e^{-\frac{t}{R_1 \cdot C}} + \frac{t \cdot U_b}{R_1} \quad (2.20)$$

As result:

$$i_c(t) = \frac{-1}{R_2} \cdot e^{-\frac{t}{R_1 \cdot C}} + \frac{U_b}{R_1} \quad (2.21)$$

	Solution without albumin	Solution with albumin
$R_1 C$	0.131 ms	0.147 ms

Tab 2.2: The capacitive current decay constant for both the solution with and without albumin

Concluding from that EIS measurement, the capacitive currents of a potential jump experiment (chronoamperometry) decays very rapidly (in maximum 0.15 ms). Therefore, the chronoamperometric current measured is almost completely a Faraday current. Although the error due to the parameter estimation (Fig 2.15) is assumed to be considerable, the capacitive currents are neglected in the following.

The Faraday Current:

The Faraday current is the interesting current in our electrolysis experiment. It decays as described in the Cottrell equation (2.20).

The Cottrell equation states that the current measured depends on the rate at which the redox active agents diffuse to the electrode or away from the electrode.

This equation is applicable to calculate an I(t) curve if a single diffusion process dominates the whole reaction.

The diffusion controlled current is given by the relation:

$$i = \frac{nFAc_j^O \sqrt{D_j}}{\sqrt{\pi t}} \quad (2.22)$$

Where

- i Current, in unit A
- n Number of electrons (to reduce/oxidize one molecule of analyte j, for example)
- F Faraday constant (96 485 C/mol)
- A Area of the electrode (cm²)
- c_j^O Initial concentration of the reducible analyte (mol/cm³)
- D_j Diffusion coefficient for species j (cm²/s)

In the case of water electrolysis, the reactant is assumed to be H₂O and the products are H⁺ and the dissolved oxygen O₂.

The current rises instantaneously after the change in voltage and then begins to drop as a function of time. Immediately after the step, H₂O is converted into H⁺ and O₂ and a large current begins to flow. With increasing time however, the steep concentration gradients of the products decrease and the diffusion process become slower. Since the whole Faraday reaction is diffusion controlled, the Faraday current decrease concomitantly. The measured current was inserted in the COMSOL model as an interpolated function, as shown in Fig 2.16.

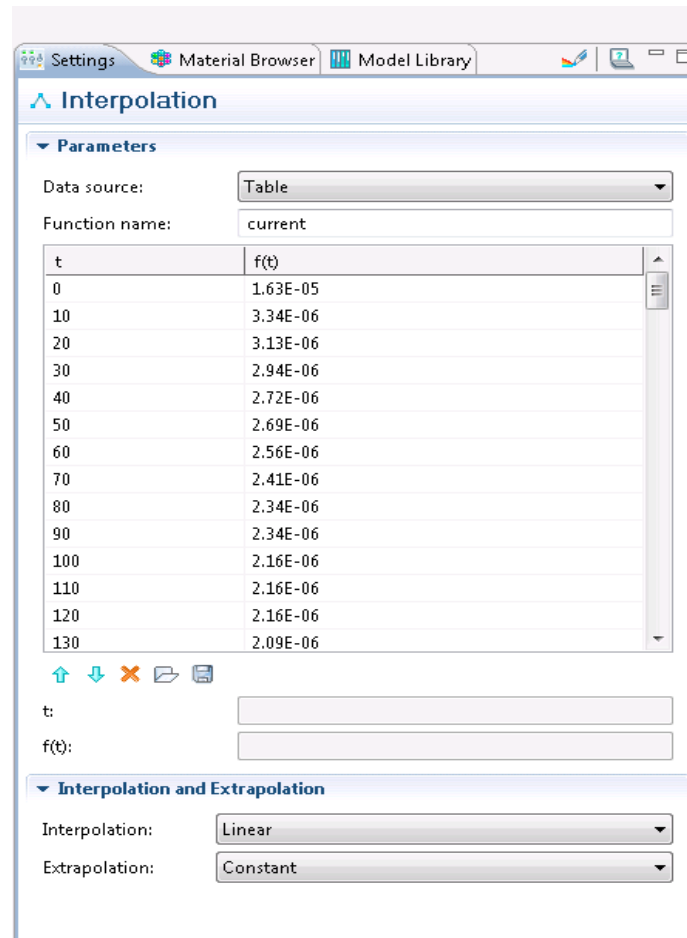


Fig 2.16: Implementation of the measured current as an interpolated function in COMSOL

2.7 The buffer effects

Buffers are able to retain almost constant pH when small amounts of acid or base are added. The quantitative measure of this resistance to pH changes is called buffer capacity and defined by the following relationship:

$$\beta = - \frac{\partial c_{(\text{H}_3\text{O}^+)}}{\partial \text{pH}} \quad (2.23)$$

Two buffers have been used for the validation experiment (see 2.5.1). The total buffer capacity of both the buffer solution with and without albumin was measured by titration of the medium with a 1 M HCl solution in 15 μl increments. Thus, the concentration change of H^+ ions (Δc_{added}) in each step is:

$$c = \frac{15 \cdot 10^{-6} \text{ mol} \cdot \text{L}^{-1}}{0.08 \text{ L}} = 1.81 \cdot 10^{-4} \text{ mol L}^{-1} \quad (2.24)$$

METHODS AND EXPERIMENTAL

The measurements took place at room temperature. The results are presented in the following tables:

HCL in μL	0	15	30	45	60	75	90	165	180	195	210
pH	pH0	pH1	pH2	pH3	pH4	pH5	pH6	pH7	pH8	pH9	pH10
pH-Values	7.44	7.38	7.24	7.11	7.01	6.9	6.8	6.71	6.62	6.54	6.33

Tab 2.3: Experimental determination of the buffering capacity in the medium without addition of albumin

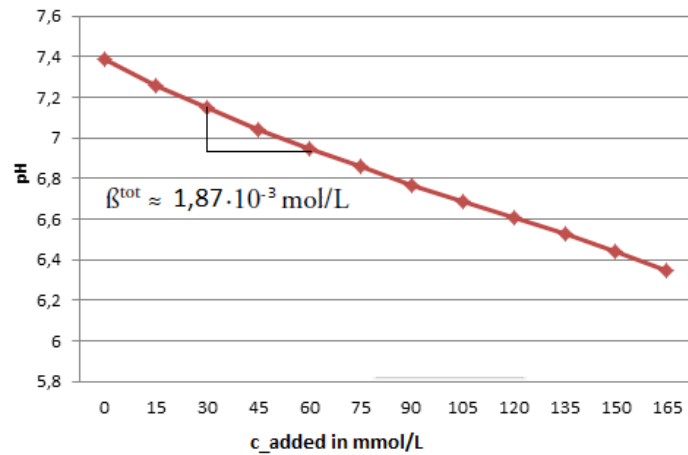


Fig 2.17: Titration curve of the medium without addition of albumin

HCL in μL	0	15	30	45	60	75	90	165	180	195	210
pH	pH0	pH1	pH2	pH3	pH4	pH5	pH6	pH7	pH8	pH9	pH10
pH-Werte	7.39	7.33	7.27	7.22	7.17	7.13	7.08	7.03	6.99	6.91	6.86

Tab 2.4: Experimental determination of buffer capacity in the culture medium with addition of albumin

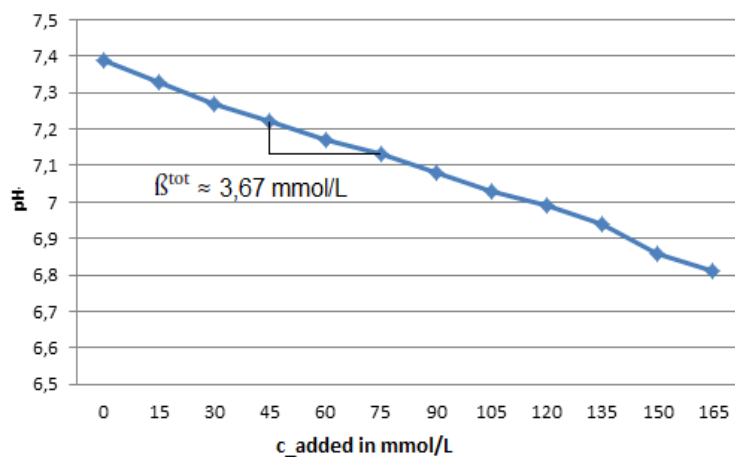


Fig 2.18: Titration curve of the medium with addition of albumin

The titrations result for both cases is approximately a linear relationship between the pH and c_{added} . Therefore, the buffer capacity is assumed to be constant in the relevant range of pH values (i.e 7.4 to 6.5). Values of 1.875 mmol/L and 3.67 mmol/L for both the solution with and without albumin were obtained by regular regression of the slope of $(\Delta\text{pH} / \Delta c_{\text{added}})$.

The effect of the buffer capacity on the spacio-temporal distribution of pH is twofold: First, it reduces the reaction rate and therefore the flux. Second, the buffering substances decrease the effective diffusion constant of protons, according to [3].

2.7.1 Buffer effect on the reaction rate

The buffer capacity reduces the proportion of the protons remaining as “free protons” in the medium after being released from the electrode. The rest part of the protons is bound to buffering species in solution. This is implemented by multiplication of the actual cellular proton release rate R with a factor Q defined as:

$$Q = \frac{\partial c_{\text{free}}}{\partial c_{\text{H}_3\text{O}^+}} \approx \ln 10 \cdot \beta^{-1} \cdot c_{\text{free}} = \ln 10 \cdot \beta^{-1} \cdot 10^{-\text{pH}} \quad (2.25)$$

Where

c_{free} the concentration change of the free protons relevant for the pH value

$c_{\text{H}_3\text{O}^+}$ the concentration change of the protons added by anodic electrolysis

Calculated for both solutions with and without albumin, Q has the following expressions:

$$Q_{\text{without-Albumin}} = 1231 \cdot 10^{-\text{pH}} \quad (2.26)$$

$$Q_{\text{with-Albumin}} = 627 \cdot 10^{-\text{pH}} \quad (2.27)$$

As a result the new proton's flux with consideration of the buffer capacity is:

$$F_{\text{H}^+}(t) = \frac{Q \cdot I(t)}{A \cdot F} \quad (2.28)$$

2.7.2 Buffer effect on the diffusion coefficient

When bound to either small molecules (mobile buffer) like the phosphate ion or large proteins (fixed or immobile buffer like albumin with a diffusion constant that is very much smaller than that of small species), H^+ ions diffuse effectively with a velocity depending on the diffusion constant of that substance. Hence, the relative reduction of the proton diffusion coefficient depends on the buffer capacity, defining the ratio between free protons and bound protons. It also depends on the relative sizes of the buffering species.

Apart from the diffusion of the protons H_3O^+ , the diffusion of the hydroxide ions OH^- should be taken into consideration.

Junge et al. [3] introduced an effective diffusion constant for H^+ ions as follows:

$$D_{H_{eff}} = D_H \cdot \left[\frac{2.3 \cdot [H^+]}{\beta^{tot}} \right] + D_{OH} \cdot \left[\frac{2.3 \cdot [OH^-]}{\beta^{tot}} \right] + \frac{\sum D_i \beta_i}{\beta^{tot}} \quad (2.29)$$

Where:

D_{OH} Diffusion constant of the hydroxide ions

D_i Diffusion constant of the mobile buffers

β_i Buffer capacity of the mobile buffers

β_{tot} Total buffer capacity in buffer solutions (from mobile and fixed buffer)

If the concentration of the fixed buffer, the albumin in this thesis, increases, the total buffer capacity increases too and therefore the effective diffusion constant decreases.

β_i can be calculated by means of the Henderson-Hasselbach equation:

$$\beta_i = \ln 10 \cdot [H^+] \left(1 + \frac{[F_i^{tot}] \cdot K_{Fi}}{([H^+] + K_{Fi})^2} \right) \quad (2.30)$$

Where :

$[F_i^{tot}]$ Concentration of the mobile buffer

K_{Fi} Equilibrium constant of the buffer

The diffusion constant of the different species involved in the diffusion process are listed in Tab 2.5.

	Value	Unit
$D_{H, 25\text{ }^{\circ}\text{C}}$	$9.3 \cdot 10^{-5}$	cm^2/s
$D_{H, 37\text{ }^{\circ}\text{C}}$	$12.33 \cdot 10^{-5}$	cm^2/s
$D_{\text{phosphat}, 25\text{ }^{\circ}\text{C}}$	$0.9795 \cdot 10^{-5}$	cm^2/s
$D_{\text{phosphat}, 37\text{ }^{\circ}\text{C}}$	$1.2988 \cdot 10^{-5}$	cm^2/s
$D_{\text{OH}^-, 37\text{ }^{\circ}\text{C}}$	$10.47 \cdot 10^{-5}$	cm^2/s
D_{O_2}	$2.7 \cdot 10^{-5}$	cm^2/s

Tab 2.5: Diffusion coefficients in water

In our case, the concentration of phosphate ion species as the only mobile buffering substance is 0.116 mol/L. The equilibrium constant K_F (equilibrium between mono- and divalent phosphate, $\text{HPO}_4^{2-}/\text{H}_2\text{PO}_4^-$) is $6.2 \cdot 10^{-8}$, thus β_{phosphat} is about 3.6 mmol/L.

It results, that D_{eff} is $\approx 0.05 \cdot D_H$ in the solution without albumin and $\approx 0.016 \cdot D_H$ in the solution with albumin.

2.8 Implementation of the sensor response time

2.8.1 Operation mode of the optochemical sensors

As described above, each well of the plates contains two optochemical sensor spots (PreSens GmbH, Regensburg), for pH and dissolved oxygen.

In optochemical sensors, the solution interacts with an indicator dye and changes its optical properties. The result is an absorbance change, a spectral shift or another change in fluorescence (or luminescence) properties (life time, polarization...).

The used oxygen sensor measures the fluorescence decay time of the immobilized fluorophore to determine the concentration of the dissolved oxygen:

$$\tau = f([\text{O}_2]) \quad (2.31)$$

In technical terms, this delay is the phase angle between the exiting and emitted signal. This phase angle is shifted as a function of the analyte concentration.

The relation between decay time τ and the phase angle Φ is shown by the following equation:

$$\tau = \frac{\tan \Phi}{2\pi \cdot f_{mod}} \quad (2.32)$$

Where

T The luminescence decay time

Φ The phase angle

f_{mod} The modulation frequency

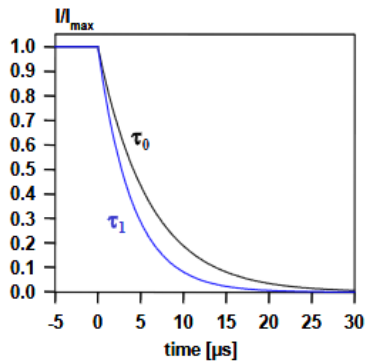


Fig 2.19: Schematic of the single exponential decay ($t_0 > t_1$)

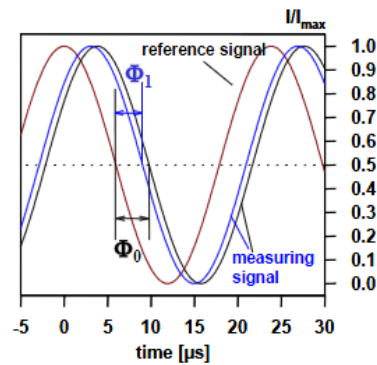


Fig 2.20: The fluorophore is excited with a sinusoidally modulated light. Emission is delayed in phase expressed by the phase angle Φ relative to the excitation signal, caused by the decay time of the excited state

For the case of the pH sensor, the relation between the phase angle Φ and the pH value is given by the equation:

$$\Phi = \frac{A_1 - A_2}{1 + e^{\frac{pH - pH_0}{dpH}}} + A_2 \quad (2.33)$$

Where

A1 The maximal value of Φ (56.31°)

A2 The minimum value of Φ (20.45°)

pH_0 The minimum value of pH (7.1984)

dpH Slope at the turning point of the curve (0.8149)

Fig 2.21 represents a calibration of a pH sensor: The phase angle is measured in different buffer solutions with adjusted pH values (red circles). A sigmoid curve showing the pK_s value of the indicator dye at the inflection point is fitted to the experimentally determined values (with the so called non linear fitting method, the Boltzmann Fitting), yielding a calibration line. The calibration results in a linearization of the sensor output with increasing errors at pH values far from the dye's pK_s value.

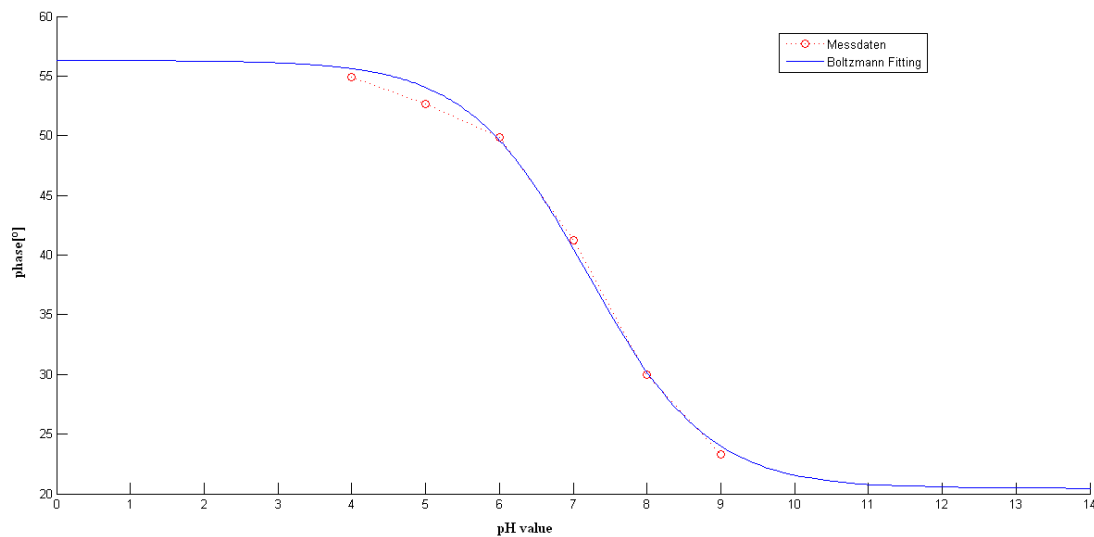


Fig 2.21: Relationship between the measured pH and the phase angle

The measurement of the luminescence decay time, an intrinsically referenced parameter, has many advantages compared to the conventional intensity measurement methods:

First of all, the decay time does not depend on fluctuations in the intensity of the light source and the sensitivity of the detector.

Second, the decay time is not influenced by signal loss caused by fiber bending or by intensity variations caused by changes in the geometry of the sensor.

Moreover, the decay time is largely independent of the concentration of the indicator in the sensitive layer. Thus, photo bleaching and leaching of the indicator dye has no direct influence on the measuring signal.

Finally, the decay time is not influenced by variations in the optical properties of the sample including turbidity, refractive index and coloration.

2.8.2 Modeling of the sensors

The response time is an important characteristic feature of every sensor: The sensor does not change its output immediately when an instantaneous input parameter change occurs. Rather, it changes to the new state over a period of time, called the response time. The response time can be defined as the time required for a sensor output to change from its previous state to a final settled value within a tolerance band of the correct new value. Typically values of t_{63} or t_{90} are given, describing the time necessary to reach 63% or 90% of the signal change after an input parameter jump. The process resembles a capacitor charging time through a resistance.

It was observed that the sensor do not change its output state immediately when an input parameter change occurs. Rather, it changes to the new state over a period of time, called the response time. The response time can be defined as the time required for a sensor output to change from its previous state to a final settled value within a tolerance band of the correct new value, in a similar way to a capacitor charging through a resistance.

The sensor response time depends on the diffusion rate of protons and oxygen molecules, respectively through the sensor layer. Since the diffusion velocity of protons depends on the composition of the buffer (see section 2.7), immobile buffering species such as proteins would further decrease the diffusion constant and increase the response time.

In the Bachelor thesis of Mrs. Xiaroui Zhang, a zero response time was assumed. However, the observed response t_{63} time is about 15s +/- 30 s for the oxygen sensor and 100 +/- 60 s for the pH sensor. The response times of pH sensors has been experimentally analyzed in a previous practical work [11].

As it will be shown in the following sections, the considerable response time of the pH sensor results in a loss of resolution accuracy and a marked distortion of real sensor graphs (Fig 2.22).

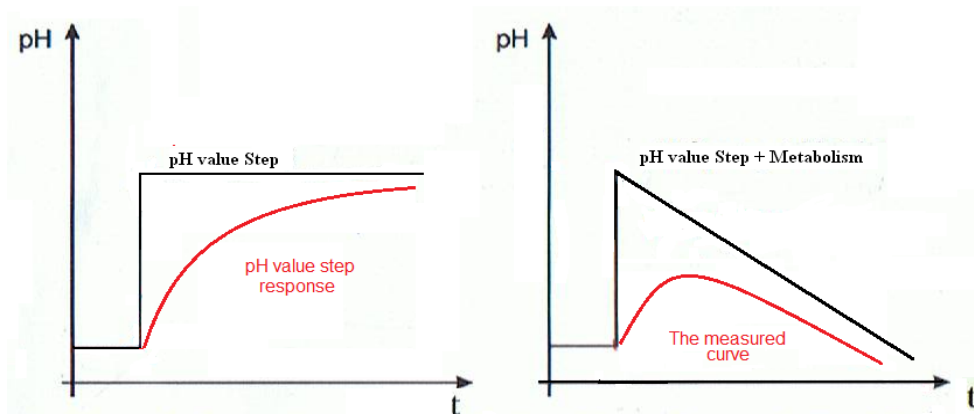


Fig 2.22: Discrepancy between the ideal curves (in black) and the measured ones (in red). The left Graph is a sketch showing the sensor response to a step of pH. The right graph is the response to a step of pH (resulting, e.g. from an instantaneous medium exchange in the test plate) followed by a linear pH decrease caused by the cell metabolic activity (according e.g. to a constant cell metabolic rate)

For the reason stated above, an output-input description of the pH-Sensor should be found to explicitly define the relation between the input and output terminals, i.e. between the real pH value and the measured one.

The pH-Sensor can be modeled as a Linear Time Invariant System (LTI System); such a system has the following properties:

-**Linearity** means that the relationship between the input and the output of the system is a linear map: If input $x_1(t)$ produces response $y_1(t)$ and input $x_2(t)$ produces response $y_2(t)$ then the scaled and summed input $a_1 x_1(t) + a_2 x_2(t)$ produces the scaled and summed response $a_1 y_1(t) + a_2 y_2(t)$ where a_1 and a_2 are real scalars. Fig 2.21 shows that the pH value is an approximatively linear function of the phase angle (the primary measured parameter) within the analyzed range of pH. Generally, the calibration leads to a linearized system. However, this is only right for the pH value and not for the protons concentration.

For the case of the O_2 sensor, the system is considered to be linear after sensor calibration with regard to the concentration, since the oxygen concentration is the calibrated parameter.

-**Time invariance** means that whether we apply an input to the system now or T seconds from now, the output will be identical except for a time delay of T seconds. That is, if the output due to input $x(t)$ is $y(t)$, then the output due to input $x(t-T)$ is $y(t-T)$.

This is obviously true for the case of the sensors.

As a result the pH sensor can be considered as an LTI System with regard to the pH value.

The oxygen sensor is an LTI System with regard to the concentration.

The fundamental result in LTI system theory is that any LTI system can be characterized entirely by a single function called **the system's impulse response**. The output of the system is simply the convolution of the input to the system with the system's impulse response (Fig 2.23). This method of analysis is often called the time domain point-of-view. The same result is true for discrete-time linear shift-invariant systems in which signals are discrete-time samples, and convolution is defined on sequences.

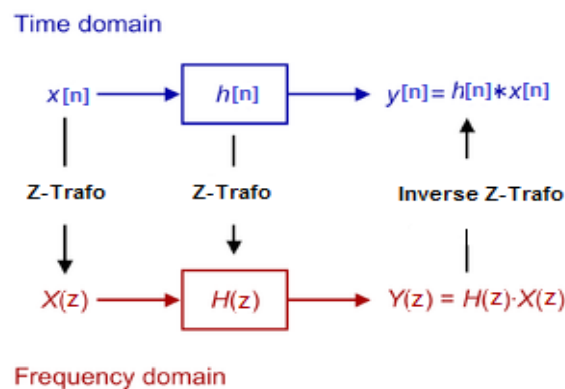


Fig 2.23: Relationship between the time domain and the frequency domain for LTI Systems

To summarize, the convolution formula provides us with a mean for computing the response of a relaxed, linear time invariant system to any arbitrary input signal $x(n)$, where $x(n)$ is the input signal to the system, $h(n)$ is the impulse response of a system and $y(n)$ is the output of the system in response to the input signal $x(n)$:

$$y(n) = x(n) * h(n) \quad (2.34)$$

$$= \sum_{k=-\infty}^{+\infty} h(k) \cdot x(n - k)$$

In this work, the sensor is simulated as a discrete LTI system. The input signal corresponds to the simulated data and the output signal is an approximation of the measurement values.

2.8.3 Determination of the sensor's impulse response

$h(t)$ is the output of the sensor when the input is a Dirac delta function $\delta(t)$. Since generating a pH or oxygen impulse is physically impossible, $h(t)$ is obtained by differentiation of the step response $s(t)$ which is much easier to generate.

$$\frac{d\delta(t)}{dt} = u(t) \quad (2.35)$$

$$\frac{ds(t)}{dt} = h(t) \quad (2.36)$$

Oxygen sensor impulse response

To obtain an oxygen step response, we generate an oxygen jump from a solution (1) with an oxygen concentration lower than the saturation value, to a solution (2), which is oxygen saturated. That occurs by pipetting of 500 μL of solution (1) into the culture well, aspirating that volume after settling of the sensor signal and then quickly introducing of solution (2).

Solution (1) has been prepared by gassing N_2 into it. The solution equilibrates with 0% oxygen atmosphere or at least with an atmosphere with an atmosphere with decreased oxygen partial pressure.

According to Henry's law (stating that the concentration of a dissolved gas in a liquid at a particular temperature is proportional to the pressure of that gas above the liquid), solution (1) will acquire a lower oxygen concentration.

The oxygen step response (Fig 2.24) shows a short sensor response time t_{63} of nearly 15 s. In view of the usual time scale of an experiment (1200 s), the response time is neglected. It is assumed that, the input signal (the real dissolved oxygen concentration $[\text{O}_2]$) is entirely transmitted to the output (the measured $[\text{O}_2]$).

METHODS AND EXPERIMENTAL

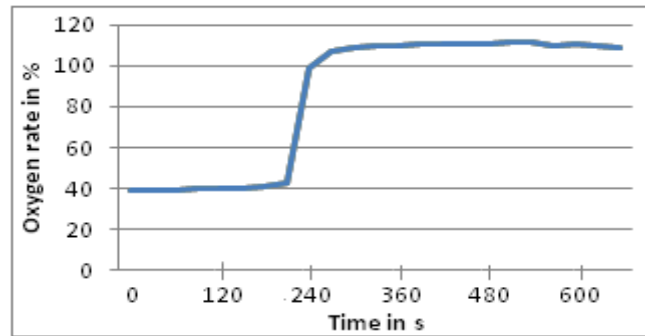


Fig 2.24: Step response of the oxygen Sensor showing a very short response time of ≈ 15 s

pH sensor response time:

The experimental generation of the pH step response time is the same as the one described above for the case of the oxygen sensor. The obtained curves for the case with and without addition of albumin are shown below:

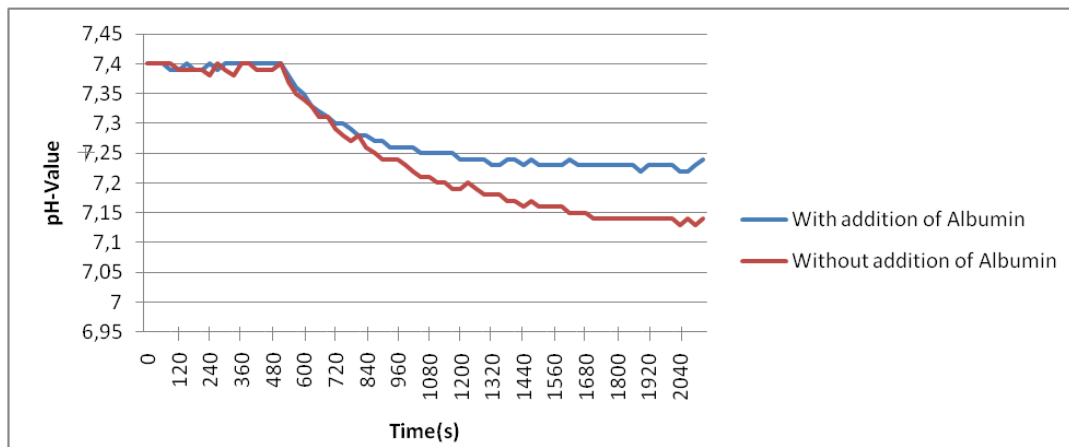


Fig 2.25: The pH sensor step responses for the case of the solution with and without albumin

METHODS AND EXPERIMENTAL

Once the measurement values are interpolated, the sensor step response was found to obey the following expression:

$$s(t) = pH_f + \Delta pH \cdot e^{-\frac{t}{\tau}} \quad (2.37)$$

For $t = 0$ $s(t) = pH_i = pH_f + \Delta pH$

For $t \rightarrow +\infty$ $s(t) = pH_f$

Where:

pH_i The initial pH value

pH_f The final pH value

ΔpH The pH value decrease

τ The time constant corresponding to t_{63}

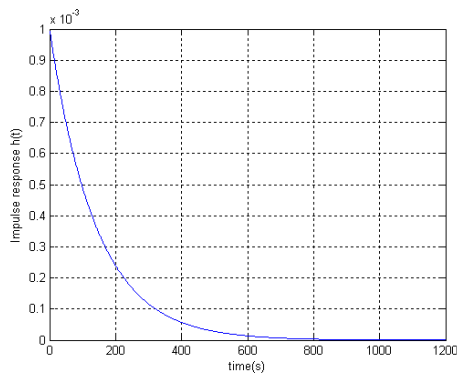
As a result:

$$h(t) = \frac{s(t)}{dt} = \frac{\Delta pH}{\tau} \cdot e^{-\frac{t}{\tau}} \quad (2.38)$$

The obtained response times are 140s for the case of the solution without addition of albumin and 170 s for the case of the solution with addition of albumin. The corresponding impulse responses are shown in Fig 2.26.

(a) Without addition of albumin

$$h(t) = (0.14/140) \cdot \exp(-t/140)$$



(b) With addition of albumin

$$h(t) = (0.08/170) \cdot \exp(-t/170)$$

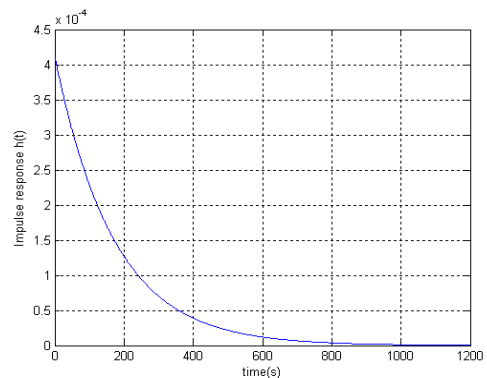


Fig 2.26: Impulse response of the pH sensor for the case of (a) a solution with addition of albumin, (b) a solution without addition of albumin

A statistic of the arithmetic average and variance of t_{63} shows that it varies from one well to another in the same multiwall plate. It is also detected that it remarkably differs from one plate to another. That's why it is recommended to measure the response time of each sensor individually for each well each time the determination of the impulse response is required.

2.8.4 Implementation of the sensor response time in the diffusion-reaction model

Since the input pH values are discrete values $pH[n]$ ($pH[n] = pH[nT]$, $n \in \mathbb{IN}$, T the sampling Period), calculated by COMSOL at discrete times, the sensor impulse response should be transformed into a discrete function too.

The resulting formal for the sensor-response time is:

$$h[n] = \sum_0^{1200} h_k \cdot \delta[n - n_k] = \frac{\Delta pH}{\tau} \cdot e^{-\frac{n}{\tau}} \quad (2.39)$$

The frequency response is obtained by applying the z-transform to $h[n]$ (2.39).

The z-transform of a discrete time signal $x[n]$ is defined as the power series:

$$X(z) = \sum_{-\infty}^{+\infty} x[n] \cdot z^{-n} \quad (2.40)$$

Where z is a complex variable. The relation (2.40) is called the direct transform because it transforms the time domain $x[n]$ into its complex plane representation $X(z)$. For convenience, the z-transform of a signal $x(n)$ is denoted by: $X(z)=Z\{x[n]\}$.

As result:

$$H(z) = Z - Trafo(h[n]) \quad (2.41)$$

$$\begin{aligned} &= \sum_{-\infty}^{+\infty} h[n] \cdot z^{-n} \\ &= \frac{\Delta pH}{\tau} \frac{z}{z - e^{-\frac{T}{\tau}}} \end{aligned}$$

METHODS AND EXPERIMENTAL

The approximation of the measured values is $y[n]$, obtained by the discrete convolution of $x[n]$ (the discrete pH value obtained from COMSOL simulation results) with $h[n]$:

$$y[n] = x[n] * h[n] \quad (2.42)$$

$$y[n] = \sum_0^N x[n-k] h[k] \quad (2.43)$$

Written in a matrix form, (2.37) is equal to:

$$\begin{pmatrix} y[0] \\ y[1] \\ \vdots \\ y[N+L-1] \end{pmatrix} = \begin{pmatrix} x[0] & 0 & \dots & 0 \\ x[1] & x[0] & \dots & 0 \\ \vdots & \vdots & \ddots & \vdots \\ 0 & 0 & \dots & x[L-1] \end{pmatrix} \begin{pmatrix} h[0] \\ h[1] \\ \vdots \\ h[n] \end{pmatrix} \quad (2.45)$$

Where:

L the length of the measurement signal $x[n]$ (= 1200 s)

N the order of the Impulse response (=1200 s)

3 RESULTS

3.1 Electrolysis results

The pH and dissolved oxygen measurement graphs are derived with the IMR System.

Fig 3.1 shows that the dissolved oxygen rate rises from 100% (0.214 mmol/L) to 107.05% (0.2291 mmol/L) which corresponds to an increase of 7.05% in 1200s. This is due to the oxygen generation during the anodic electrolysis.

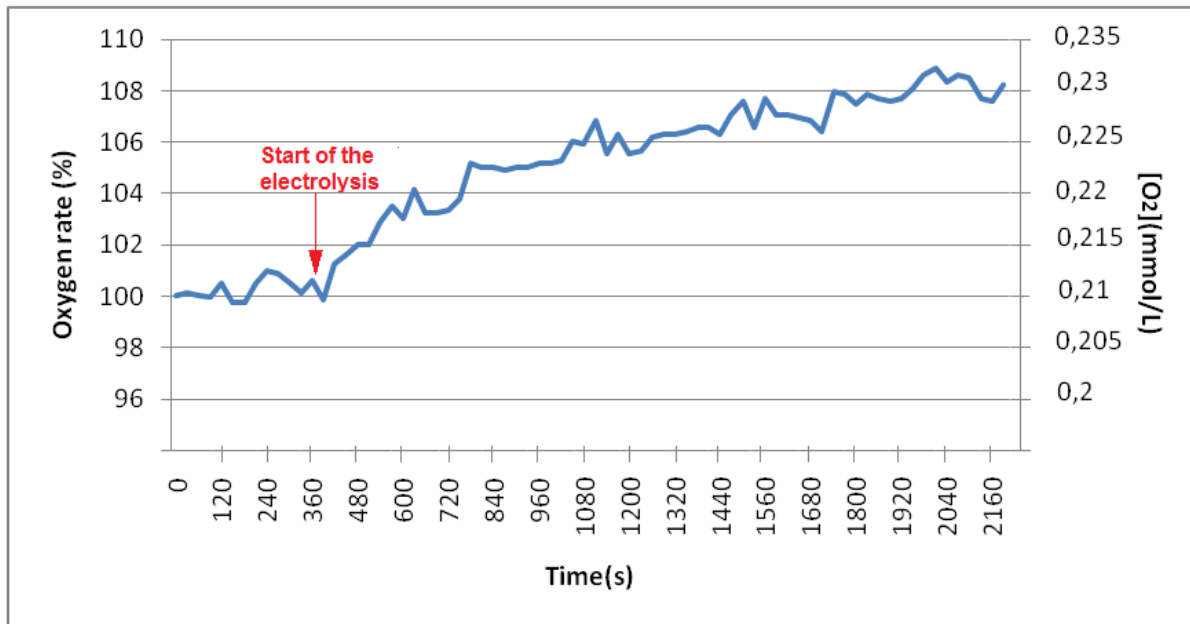


Fig 3.1: The measured dissolved oxygen given in % saturation and in concentration during an electrolysis experiment (Electrolysis start at $t=360$ s)

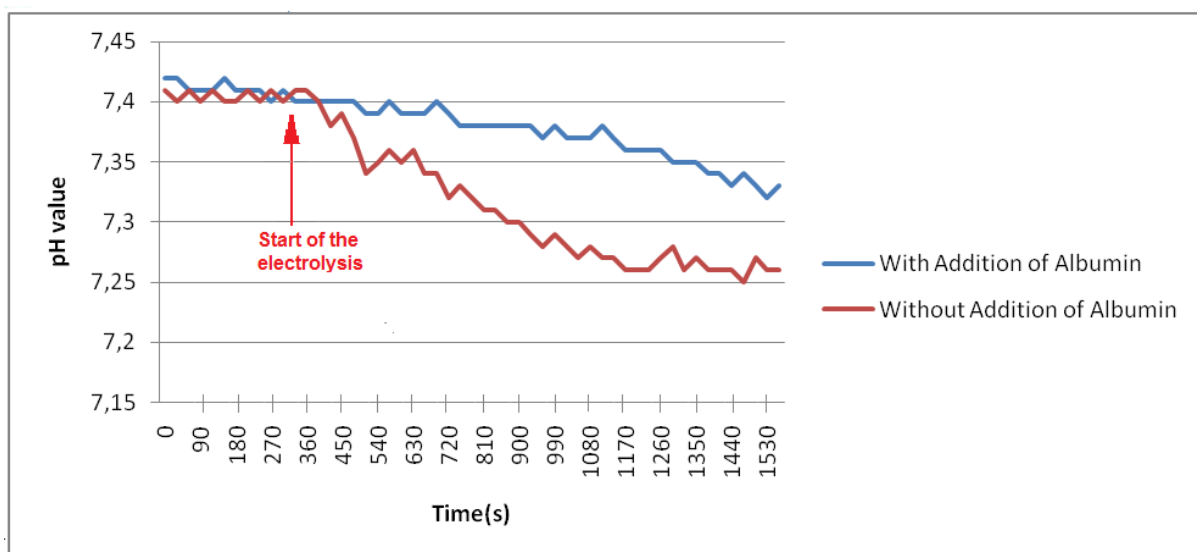


Fig 3.2: The measured pH curves during the electrolysis experiment for the case of a buffer solution with and without addition of albumin (Electrolysis start at $t=330$ s)

RESULTS

In Fig 3.2, the blue curve shows the pH decrease of the buffer solution with addition of albumin, from an initial value 7.4 before the start of the electrolysis (at $t=330$ s) to a final value of about 7.32.

This corresponds to a pH-decline of $\Delta\text{pH}=0.08$ in 1200 s. The red curve represents the pH decline for the case of a buffer solution without addition of albumin from 7.4 (at $t=330$ s) to about 7.26 after 1200 s. This corresponds to a pH-decline of $\Delta\text{pH}=0.14$ in 1200 s.

The comparison between the two curves shows that the pH decrease in the buffer solution with albumin is not only about 2.5 times less than the one in the solution without albumin, but it is also slower.

3.2 COMSOL results

COMSOL offers extensive tools for the graphical representation and analysis of simulation results. In the following sections 3.2.1 and 3.2.2 the spatial distributions of the dissolved oxygen concentration and pH after 1200 s after starting the electrolysis in a closed MRC are presented.

Based on the simulated spatio-temporal distribution of these values, the integrals on the sensor surfaces of both variables have been calculated to obtain a synthetic (simulated) sensor kinetic. For simplification, an equal contribution of each sensor surface element to the total sensor signal was assumed.

3.2.1 Simulation of the oxygen sensor readings

The special distributions of dissolved oxygen and the sensor kinetic after 1200 seconds of the start of the electrolysis in a closed MRC are shown in Fig 3.3 and Fig 3.4.

It comes out that the maximal oxygen concentration of 0.234 mmol/L is reached in the red colored area corresponding to the working electrode surface. The oxygen concentration on the surface of the opto chemical sensor is lower, since the O₂ molecules need some time to reach the sensor surface. In fact, the diffusion length, corresponding to the average distance traveled by a particle (the oxygen molecules in our case), from the point at which it is formed (the electrode surface) to the point at which it is absorbed (the sensor) is given by the formula:

$$L = \sqrt{D \cdot t} \quad (3.1)$$

Where D is the diffusion constant and t is the life time of the particles. For the case of oxygen at 25°C the O₂ molecules will need 740 s to reach the center of the sensor:

RESULTS

$$t = \frac{L^2}{2 \cdot D} = \frac{(0.1 \text{ cm})^2}{2 \cdot 2.7 \cdot 10^{-5} \cdot \frac{\text{cm}^2}{\text{s}}} = 740 \text{ s}$$

Fig 3.3 shows a three Dimensional distribution of the oxygen concentrations in the MRC after 1200 s of electrolysis. Fig 3.4 corresponds to the synthetic sensor signal, where the simulated values of oxygen saturation are integrated at the surface of the sensor.

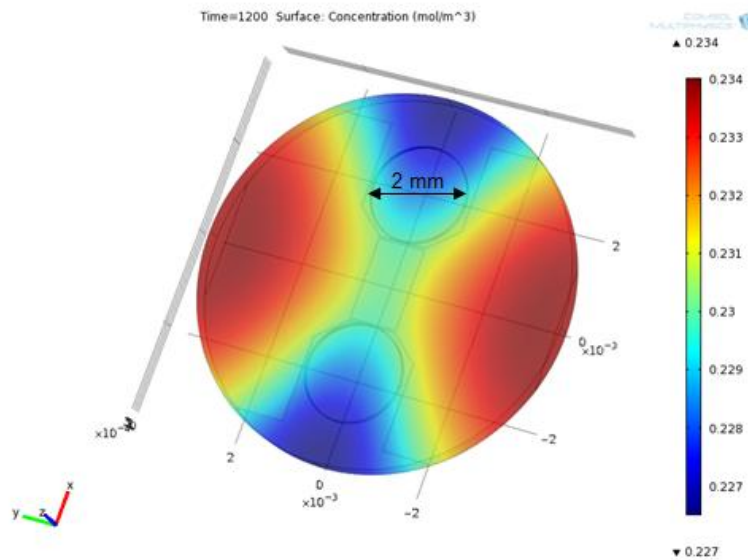


Fig 3.3: The dissolved oxygen distribution in a closed MRC 1200 s after start of the electrolysis.

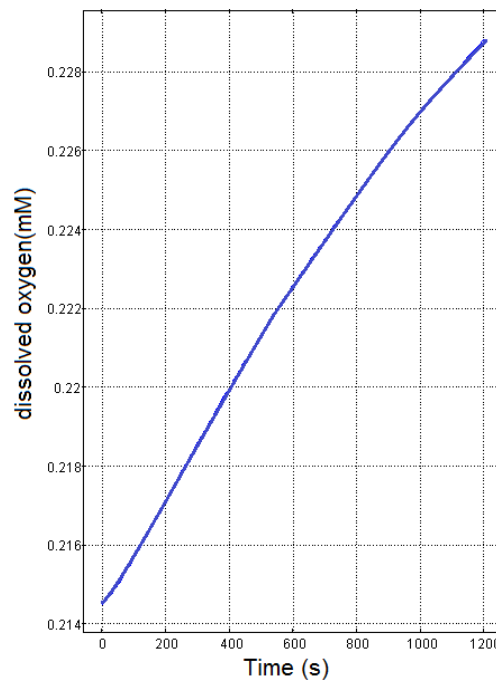


Fig 3.4: The calculated kinetic of dissolved oxygen sensor during 1200 of oxygen generation in the closed MRC

RESULTS

3.2.2 Simulation of the pH sensor readings

a) Simulation of the pH sensor readings without implementation of the sensor response time *pH sensor readings for the buffer solution without addition of albumin*

Fig 3.5 shows a simulated 3D distribution of the pH value after an electrolysis time of 1200 s. The lowest pH value of 5.4 corresponds to the highest concentration of the protons and lies on the electrode surface. The pH value on the sensor surface shows a higher value of about 5.9.

The protons will need ≈ 214 s to reach the center of the sensor:

$$t = \frac{L^2}{2 \cdot D} = \frac{(0.1 \text{ cm})^2}{2 \cdot 9.3 \cdot 10^{-5} \cdot \frac{\text{cm}^2}{\text{s}}} = 214 \text{ s}$$

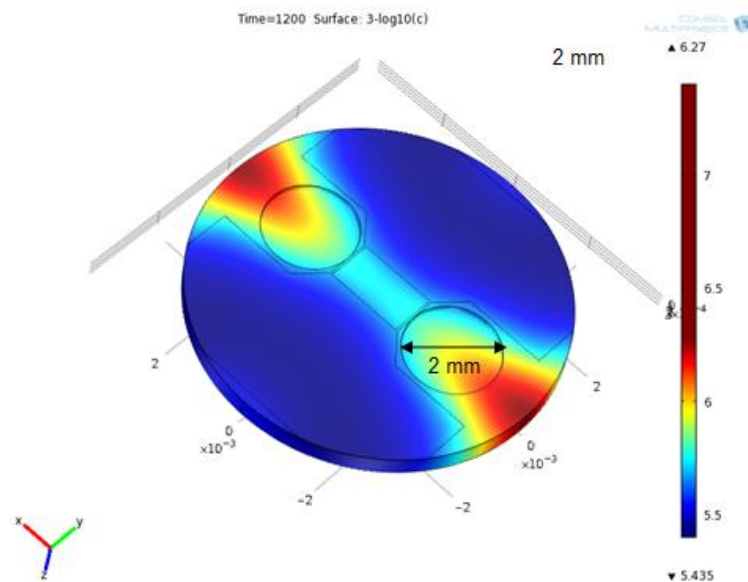


Fig 3.5: The pH value distribution in a closed MRC after 1200 s of start of the electrolysis for the case of the solution without addition of albumin

The obtained pH kinetic (Fig 3.6) was obtained by integration of simulated pH values inside the total sensor volume. The sharp initial decline of the curve at is due to the peak of the Faraday current in the first seconds of the electrolysis experiment. Due to the sensor's hydrogel matrix structure, the H^+ ion diffusion constant is assumed to equal inside and outside the sensor (personal communication of Dr. Christian Krause, PreSens GmbH, 10.06.2011).

RESULTS

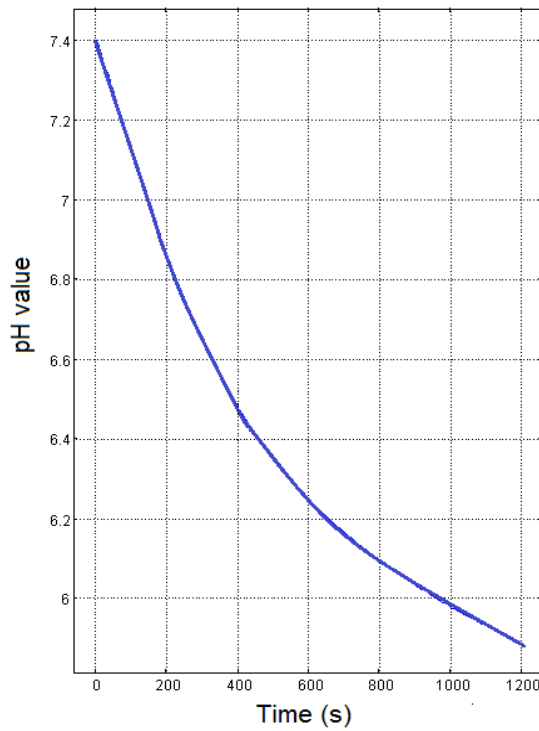


Fig 3.6: The calculated kinetic of the pH sensor during the 1200 s of the electrolysis reaction in the closed MRC for the case of the buffer solution without addition of albumin

pH-Sensor readings for the buffer solution with addition of albumin

The pH distribution (Fig 3.7) is qualitatively similar to the previous case. As expected, a smaller pH drop is calculated (Fig 3.8) which indicates the accuracy of the modeling of the buffer effect. With consideration of the buffer effect, the diffusion length is about 2 mm in 1200 s.

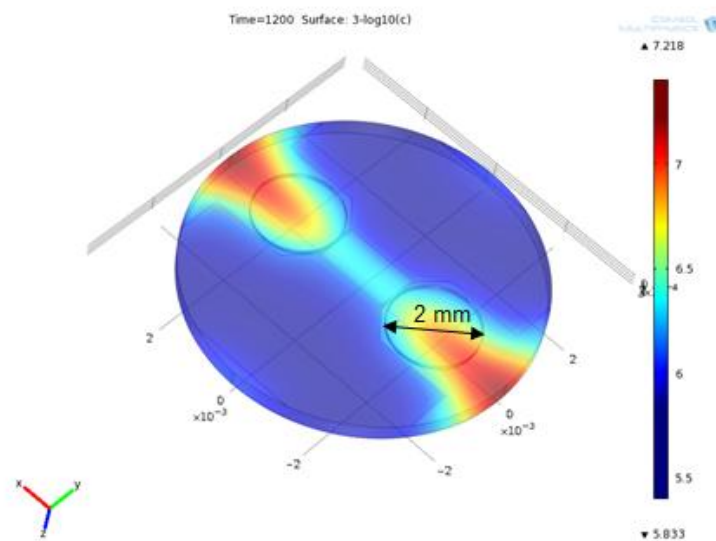


Fig 3.7: The dissolved oxygen distribution in a closed MRC 1200 s after start of the electrolysis for the case of the solution with addition of albumin

RESULTS

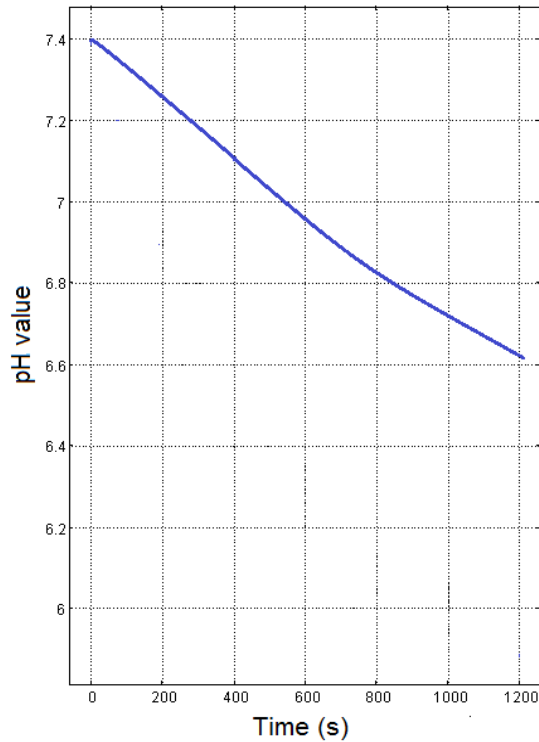


Fig 3.8: The calculated kinetic of the pH sensor during the 1200 s of the electrolysis reaction in the closed MRC for the case of the buffer solution with addition of albumin

b) Simulation of the pH sensor readings with implementation of the sensor response time *pH sensor readings for the buffer solution without addition of albumin*

The convolution of the impulse response (Fig 2.26.a) with the sensor kinetic (Fig 3.6) results in the sensor kinetic shown in Fig 3.9.

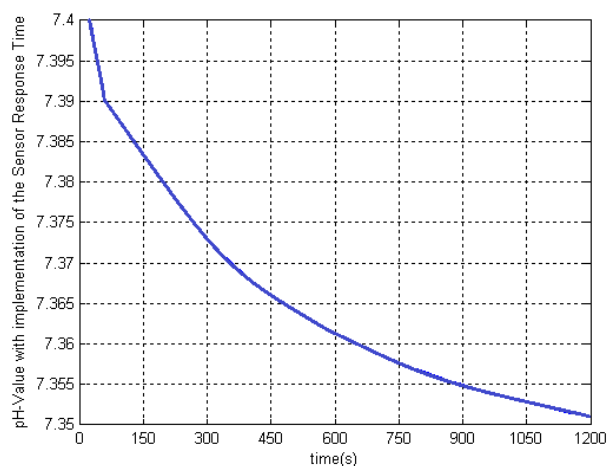


Fig 3.9: Kinetic of the pH Sensor between 0 and 1200 s with consideration of the sensor response time for the case of a buffer solution without addition of albumin and a sensor response time of 140 s.

RESULTS

pH sensor readings for the buffer solution with addition of albumin

The convolution of the impulse response (Fig 2.26.b) with the kinetic of Fig 3.8 in MATLAB results in the sensor kinetic shown in Fig 3.10.

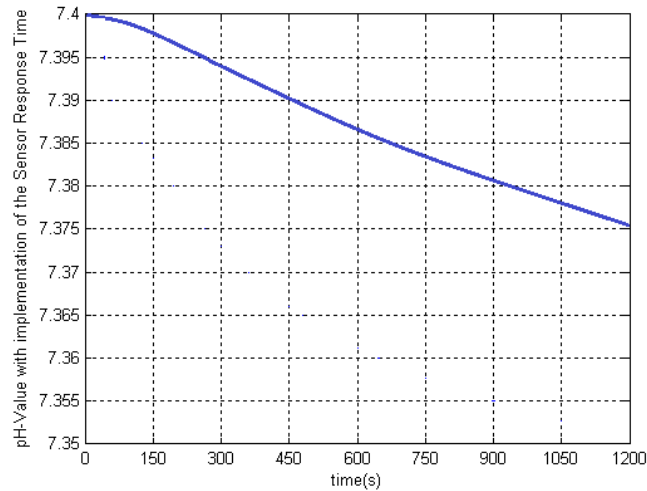


Fig 3.10: Kinetic of the pH Sensor between 0 and 1200 s with consideration of the sensor response time, for the case of a buffer solution with addition of albumin and a sensor response time of 270 s

The processed curves for both cases show a lower gradient and a lower final value (about 7.35 for the case with albumin and 7.375 for the case without albumin) compared with the kinetic obtained from the simulation. This is explained by the fact that the sensor acts like a low-pass filter. Thus, it passes low-frequency signals but attenuates signals with frequencies higher than the cutoff frequency. The cutoff frequency is about 2 Hz for the case of the frequency response $H(z)$ (Fig 3.11.a). The bandwidth of the sensor kinetic $x(t)$ resulting from the simulation is nearly 12 Hz (Fig 3.11.b). The convolution of $h(t)$ and $x(t)$ in time domain corresponds to a multiplication of $H(z)$ and $F(z)$ in frequency domain. So, all the frequencies of $X(f)$ above 2 Hz are attenuated to 0 Hz.

RESULTS

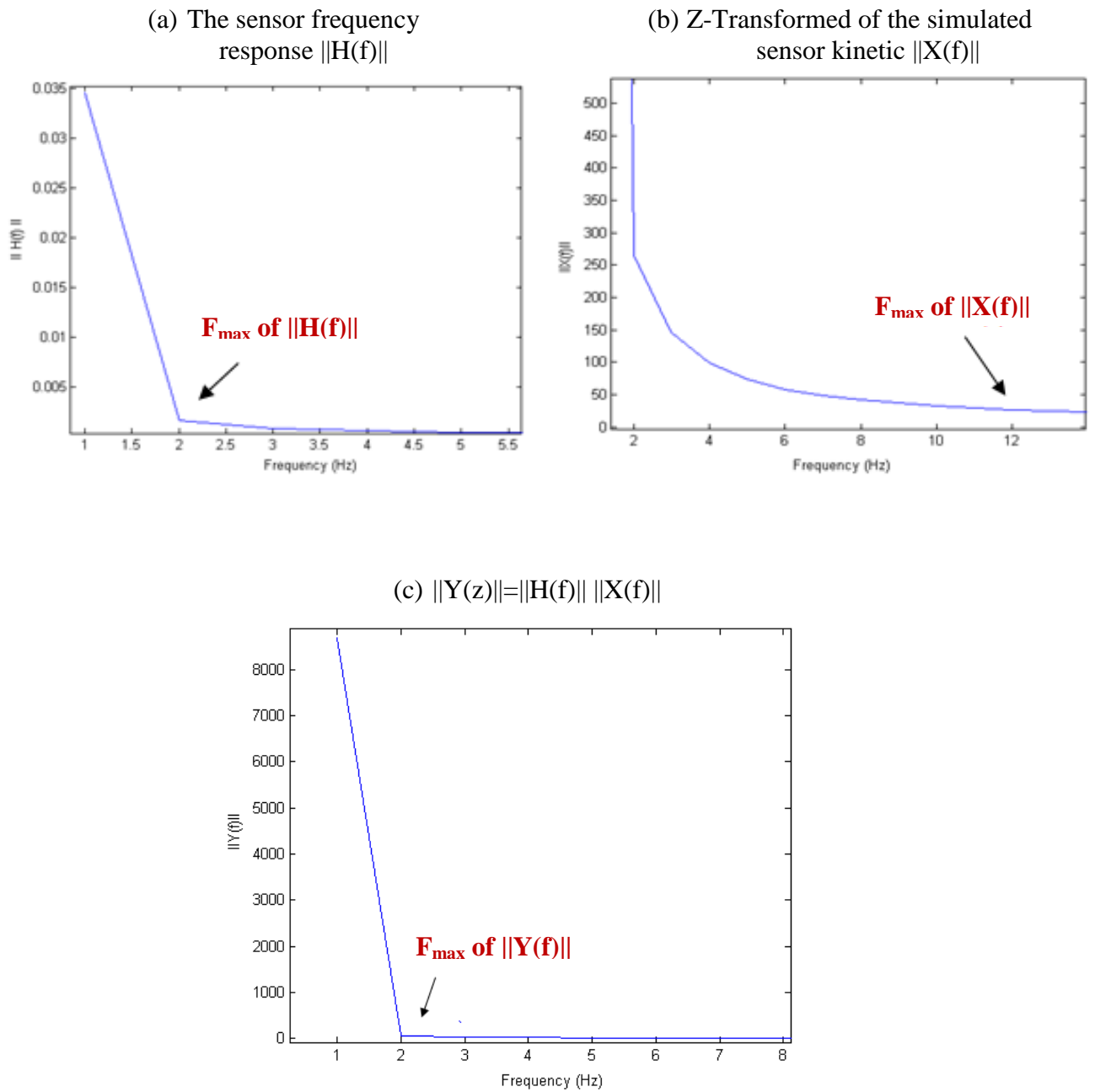


Fig 3.11: (a) Frequency response of the pH-sensor $H(z)$; (b) the Fourier Transformed of the sensor kinetic resulting from the simulation $X(z)$; (c) The convolution result of $x(t)$ and $h(t)$

4 DISCUSSION

4.1 Model verification

“**Verification**” is defined as the process of gathering evidence to establish that the computational implementation of the mathematical and physico-chemical model and their associated solution are correct.

Generally, the biological complex system is simplified to a model in which only the most influential physico-chemical processes are considered. If the simulation with the simplified model reveals a discrepancy between the predicted results and the measured ones, verification is needed to refine the model by taking more physico-chemical processes into account.

Apart from the verification of the physico-chemical model a code and calculation verification are advantageous.

“**Code verification**” [4] ensures that the mathematical model and solution algorithms are working as intended. The numerical algorithm is in the framework of finite element (FE) methods, in which discretized domains are solved iteratively until convergence criteria are met.

The errors that can occur include discontinuities, inadequate iterative convergence, programming errors, incomplete mesh convergence, lack computer round-off, etc. The code verification inquires the comparison with exact analytical solutions (most accurate but least likely to exist for complex problems). In this work the simulation was achieved with highly sophisticated software ‘COMSOL Multiphysics’, so there was no need in determining the solution of the diffusion equation explicitly.

“**Calculation verification**” [4] focuses on errors arising from the discretization of the problem domain. Errors can arise from discretization of both the geometry and analysis time. A common way to characterize discretization error in the FE method is via mesh convergence verification. This is the first step of the simulation with COMSOL.

4.2 Model validation

The two predominant types of validation are indirect and direct validation. Indirect validation utilizes experimental results that cannot be controlled by the user, such as from the literature or results of clinical studies. The experimental quality control, the sources of error, and the degree of variability are typically not known if the data are not collected by the analyst.

DISCUSSION

An example for this situation would be the validation of the reaction-diffusion model with measurements on cell cultures in the MRC where the metabolic rates are unknown.

The direct validation performs experiments, which allow an accurate determination of all the input parameters which is the case of the electrolysis experiment in this work.

By comparison of the simulated results with the real kinetic sensor data (Fig 4.1) it appears that the model can approximate the spatio-temporal distribution of the investigated physico-chemical parameters.

4.2.1 Comparison between the simulated and measured oxygen sensor kinetics

Fig 4.1 shows that the curvature and the amplitude of predicted and measured oxygen sensor kinetic are nearly the same.

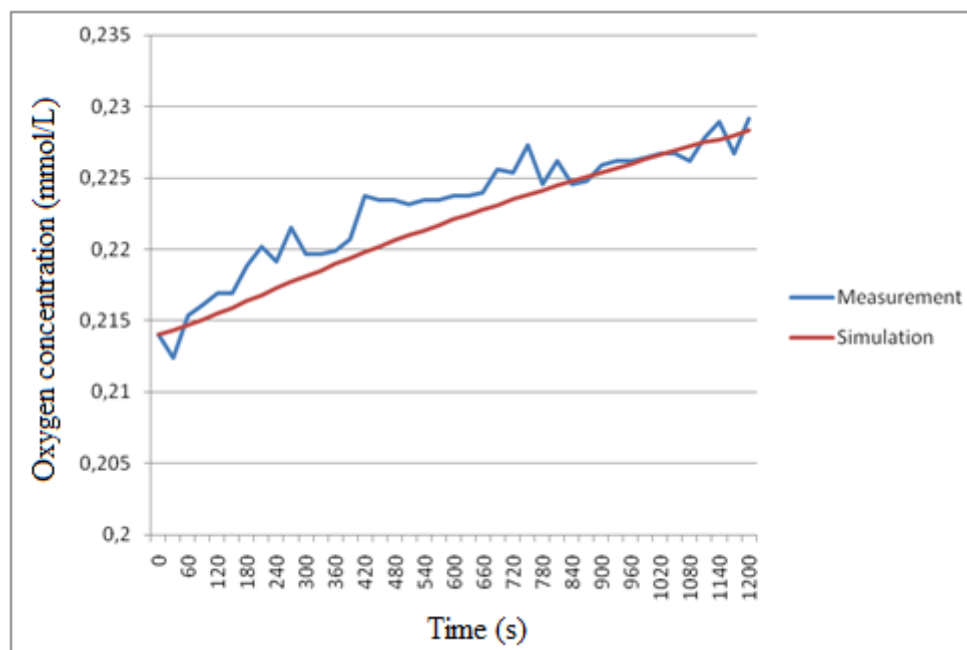


Fig 4.1: Comparison between the measured dissolved oxygen sensor kinetic and the simulated one

An overview is presented in Tab 4.1:

	Simulation	Measurement	Divergence
Initial value	0.214 mM	0.214 mM	0 mM
Final Value	0.2285 mM	0.2291 mM	-0.0006 mM
$\Delta [O_2]$ in mmol/L	0.0145 mM	0.0151 mM	-0.0006 mM
ΔO_2 in %	+ 6.7%	+ 7.05%	+ 0.28%

Tab 4.1: Comparison of the results (simulated and measured) of the dissolved oxygen

DISCUSSION

It appears that the simulation predicts the generation and diffusion of oxygen in the MRC correctly at least in a qualitative way. It is assumed that the deviation is due to errors which will be discussed in the error analysis section.

4.2.2 Comparison between the simulated and measured pH sensor kinetics

The obtained calculated pH sensor kinetics after implementation of the sensor response time closely resembles the experimentally obtained kinetics at least qualitatively, for both situations with albumin (Fig 4.2, Tab 4.2) and without it (Fig 4.3, Tab 4.3)

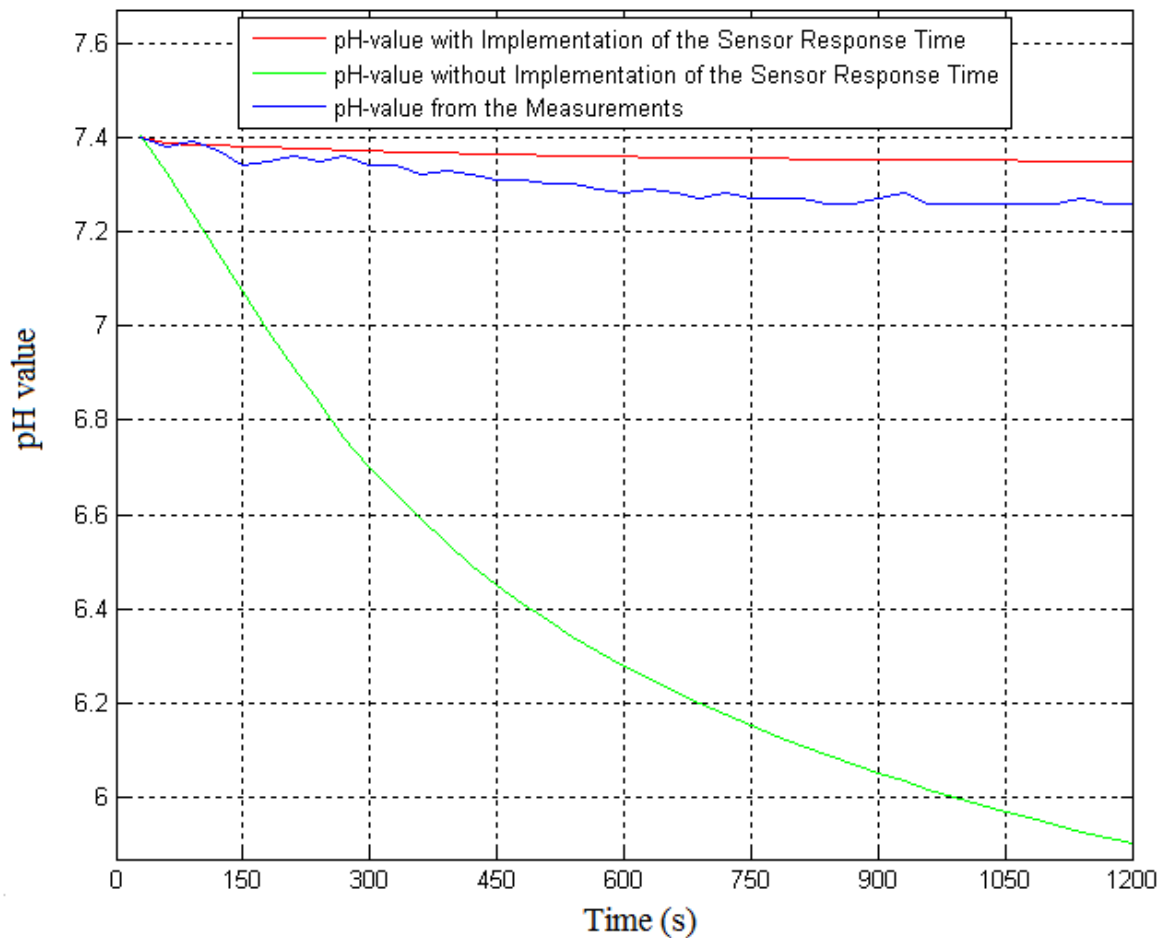


Fig 4.2: Comparison between the simulated sensor kinetic, the measured one and the one obtained after the implementation of the sensor response time for the case of the buffer solution without addition of albumin

	Simulation Result $x[n]$	Measurement Result $f[n]$	Convolution Result $y[n]$	Divergence between $f[n]$ and $x[n]$	Divergence between $f[n]$ and $y[n]$
Initial Value	7.4	7.4	7.4	0	0
Final Value	5.92	7.26	7.34	1.34	0.08
ΔpH	-1.48	-0.14	-0.06	1.34	0.08

Tab 4.2: Comparison of the results (simulated, measured and obtained after the implementation of the sensor response time)

DISCUSSION

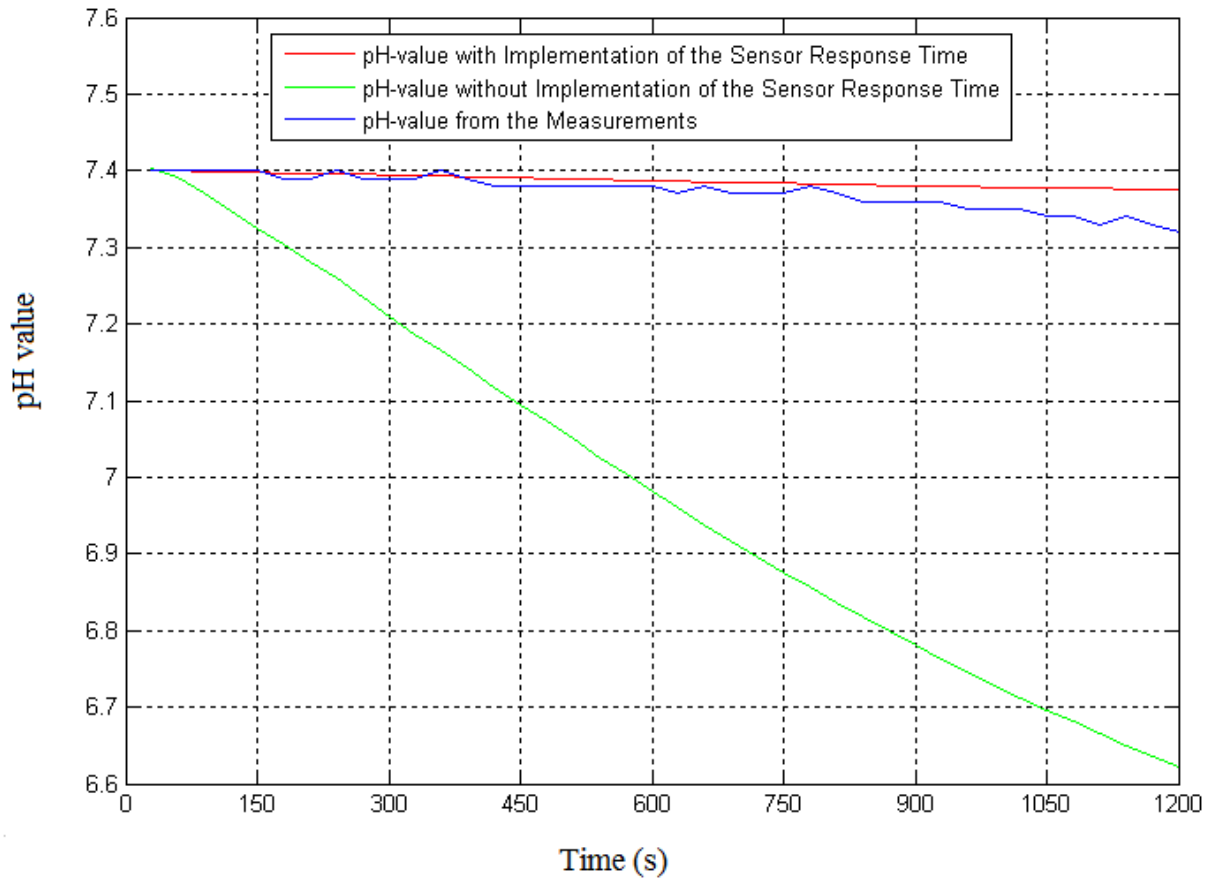


Fig 4.3: Comparison between the simulated sensor kinetic, the measured one and the one obtained after the implementation of the sensor response time for the case of the buffer solution with addition of albumin

	Simulation Result $x[n]$	Measurement Result $f[n]$	Convolution Result $y[n]$	Divergence between $f[n]$ and $x[n]$	Divergence between $f[n]$ and $y[n]$
Initial Value	7.4	7.4	7.4	0	0
Final Value	6.62	7.32	7.38	0.7	0.06
ΔpH	0.78	0.08	0.02	0.7	0.06

Tab 4.3: Comparison of the results (simulated, measured and obtained after the implementation of the sensor response time) for the case of the buffer solution with addition of Albumin.

Correlation

In statistics, the Pearson product-moment correlation coefficient is a measure of the correlation between two variables X and Y, giving a value between +1 and -1. As it approaches zero there is less of a relationship (closer to uncorrelated). The closer the coefficient is to either -1 or 1, the stronger the correlation between the variables.

DISCUSSION

The Pearson's correlation coefficient between two variables is defined as the covariance of the two variables divided by the product of their standard deviations:

$$\rho_{X,Y} = \frac{\text{cov}(X,Y)}{\sigma_X \cdot \sigma_Y} \quad (4.1)$$

With means of the correlation coefficient, the dependence between the measured and simulated sensor kinetics is examined.

For the case of the dissolved oxygen, the correlation coefficient is about 0.95.

It is about 0.97 for the buffer solution without addition of Albumin and 0.96 for the one with addition of albumin.

4.3 Sensitivity analysis:

Sensitivity analysis (SA) is the study of how the variation (uncertainty) in the output of a mathematical model can be apportioned, qualitatively or quantitatively, to different sources of variation in the input of the model.

The understanding of how the model behaves in response to changes in its inputs is of fundamental importance to ensure a correct use of the model.

The input is subject to many sources of uncertainty including errors of measurement, absence of information and poor or partial understanding of the driving forces and mechanisms. This uncertainty imposes a limit on our confidence in the output of the model.

In the case of the validation experiment, the working electrode potential has not a precise value, but a possible range of values between 1.1V and 1.8 (see section 2.5.4). Due to the use of a gold wire as a quasi-reference electrode, the potential of the working electrode vs. the electrolyte potential may vary and the degree of that instability is not known. As the measured current depends on the potential of the working electrode, its variation is a source of uncertainty.

The general procedure of the sensitivity analysis is to alter a single input parameter, while holding the others constant and investigating the effect of the change on the output.

A small variation of the working electrode potential was shown to lead to a big change in the final value of the oxygen sensor kinetics as illustrated in *Tab 4.4*.

Redox Potential	1600 mV	1350 mV	1200 mV
Final value of [O ₂]	0.7 mM	0.25 mM	0.23 mM

Tab 4.4: The influence of the working electrode variation on the final value of the dissolved oxygen concentration.

As a result, the reaction rate should be determined with a high accuracy, because a slight variation of its value results in a big variation of the output values.

Other errors can occur by the determination of the further input parameters. This may be the case of the height of the MRC, the form and position of the sensor, and the assumption of a uniform distribution of the current density on the electrode. These errors will be further discussed in section 4.4.

4.4 Error analysis

Although the simulated results appear to be a good approximation of the real reaction and diffusion process, a noticeable deviation remains. Error is defined as the difference between a simulated or experimental value and the truth. Error can arise in a number of areas, particularly inaccurate implementation of the model into a computational code or experimental errors.

4.4.1 Experimental errors

a. Signal processing errors

Calibration error

As it was mentioned in section 2.8.1, the used sensors measure the phase angle Φ between the exiting and emitted signal of the immobilized luminophore to determine the concentration of the dissolved oxygen or the pH value. However, the determination of Φ and its conversion to an oxygen concentration or a pH value isn't a precise operation (personal communication of Dipl.-Ing. Franz Demmel). For the correct readout of changes in pH, an exact determination of the slope of the phase angle vs. readjusted pH values during calibration is necessary (see Fig.22). Despite this, a fitting error will inevitably occur in view of the limited number of calibration points. This error is about ± 0.05 .

Besides of that, under-sampling and quantization errors turn out to have a big impact on the quality of the measured signal.

Under-sampling error

The under sampling error occurs when the continuous time signal is converted to a discrete one.

The Nyquist–Shannon sampling theorem states that a band limited analog signal that has been sampled can be perfectly reconstructed from an infinite sequence of samples if the sampling rate F_s exceeds $2 F_{max}$ samples per second, where F_{max} is the highest frequency in the original signal:

$$F_s \geq 2 \cdot F_{max} \quad (4.2)$$

In the case of the measurements done in the framework of this thesis using the IMS, the

sampling period is 30 s, thus $F_s = \frac{1}{T_s} = \frac{1}{30 \text{ s}} = 0.033 \text{ Hz}$

F_{max} is the band width of the Fourier transformed analog signal before the sampling. This corresponds then to the simulated sensor kinetic convoluted with the sensor impulse response. As previously mentioned, F_{max} is about 10 Hz.

Therefore, apart from the frequencies (higher than 10 Hz) filtered by the sensor impulse response, the signal values corresponding to the frequencies between $F_s/2$ and F_{max} are affected by the aliasing (i.e. the under-sampling error). This means that any frequency above $F_s/2$ or below $F_s/2$ results in samples that are identical with a corresponding frequency in the range $-F_s/2 < F < F_s/2$, which leads to ambiguities.

As a result, in this frequency range, the measured sensor curve slopes (c (O₂) vs. t and pH vs. t) are erroneous.

Another consequence of the low sampling rate is the high variance of the measured pH and O₂ sensor response times.

The worst case scenarios of the measurement of τ are shown in Fig 4.4 and Fig 4.5.

DISCUSSION

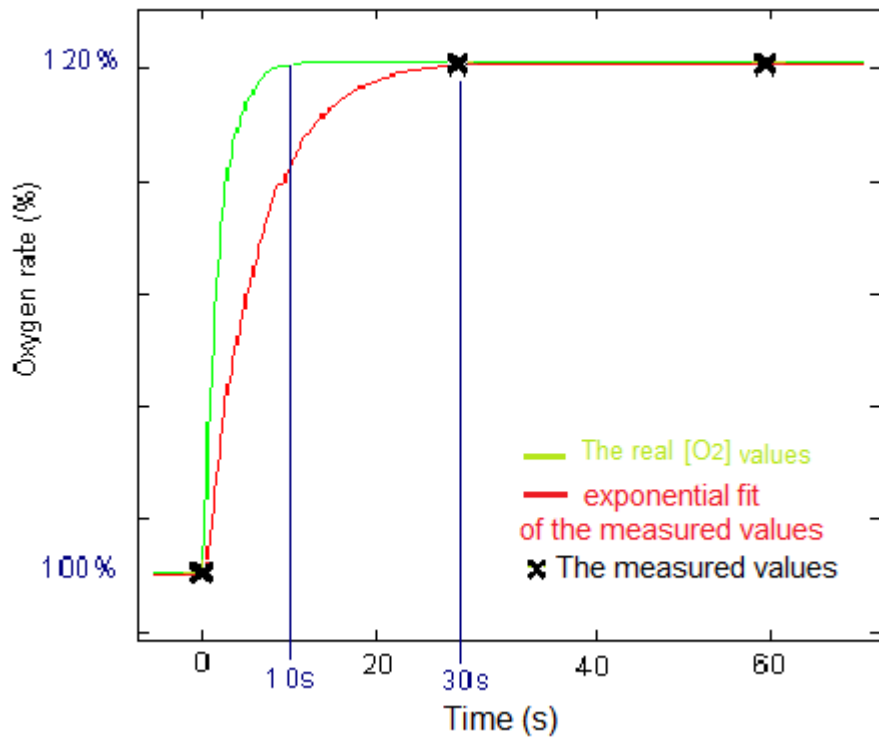


Fig 4.4: The real oxygen rate (in green) and the measured one (in red). The maximum error resulting from the low sampling rate is 30s (At the beginning of the measurement)

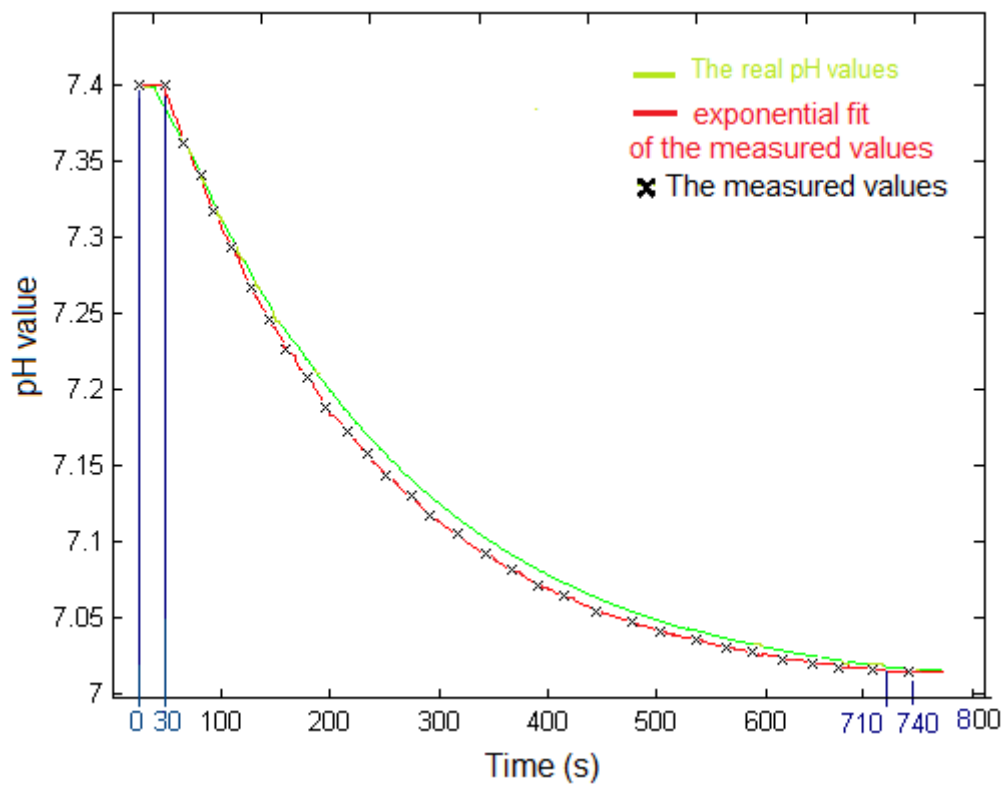


Fig 4.5: The real pH value (in red) and the measured one (in green). The maximum error Δt resulting from the low sampling rate is ± 60 s (30 s at the beginning and 30 s at the end of the measurement)

DISCUSSION

To illustrate the impact of the inaccurate determination of the pH response time, the simulated sensor kinetic for the case of both the buffer solution with and without addition of albumin is convoluted with two additional impulse responses corresponding to the worst case situation mentioned above ($t_{63}=140+60$ and $t_{63}=140-60$ for the solution without albumin and $t_{63}=170+60$ and $t_{63}=170-60$ for the solution with albumin). The obtained curves have different slopes. The red curves, with the lowest response time, yields the best approximation to the measured curves.

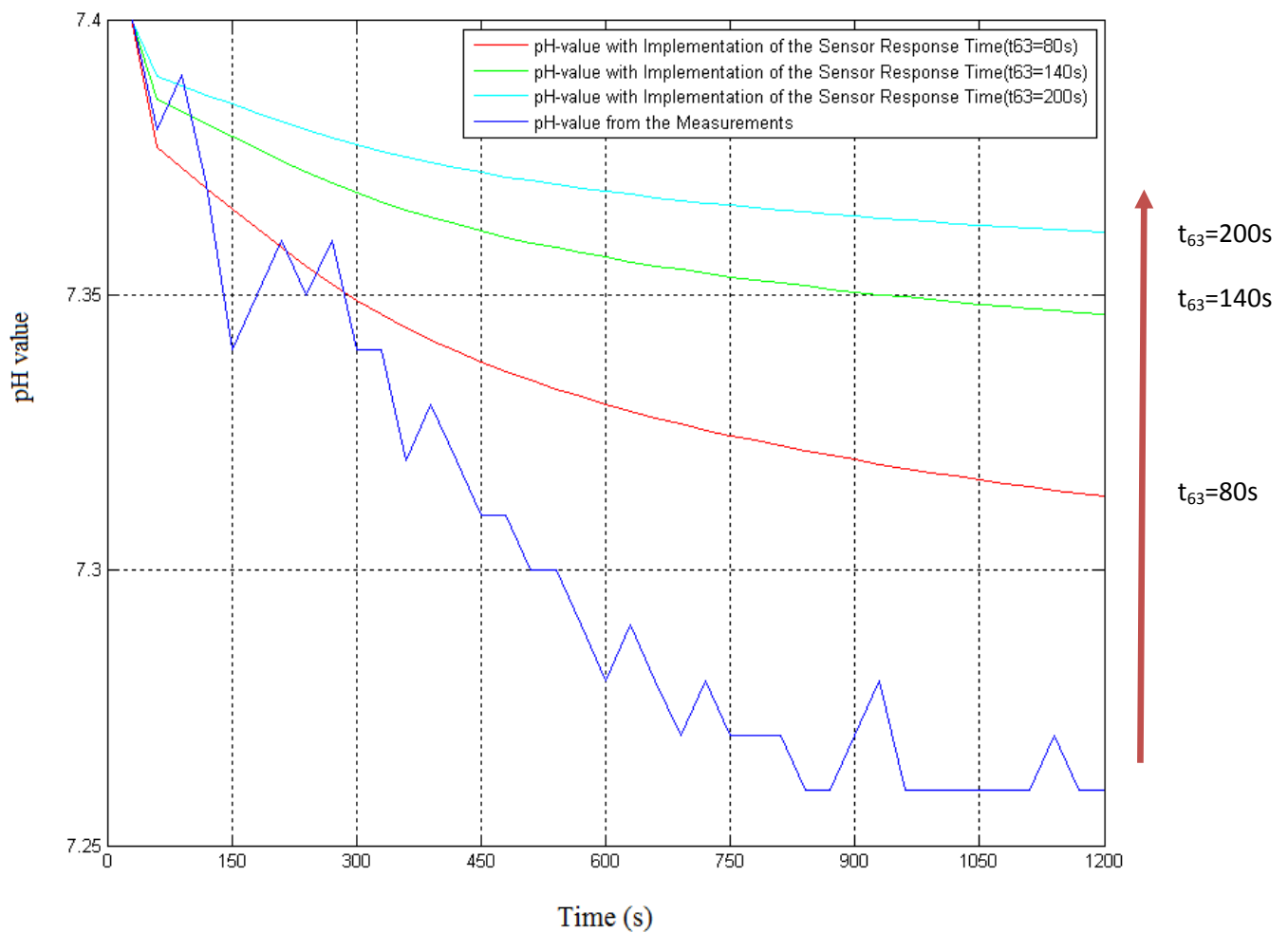


Fig 4.6: The effect of the variation of the pH-sensor response time resulting from the measurement error on the approximation of the measured sensor kinetic for the case of the solution without addition of albumin

DISCUSSION

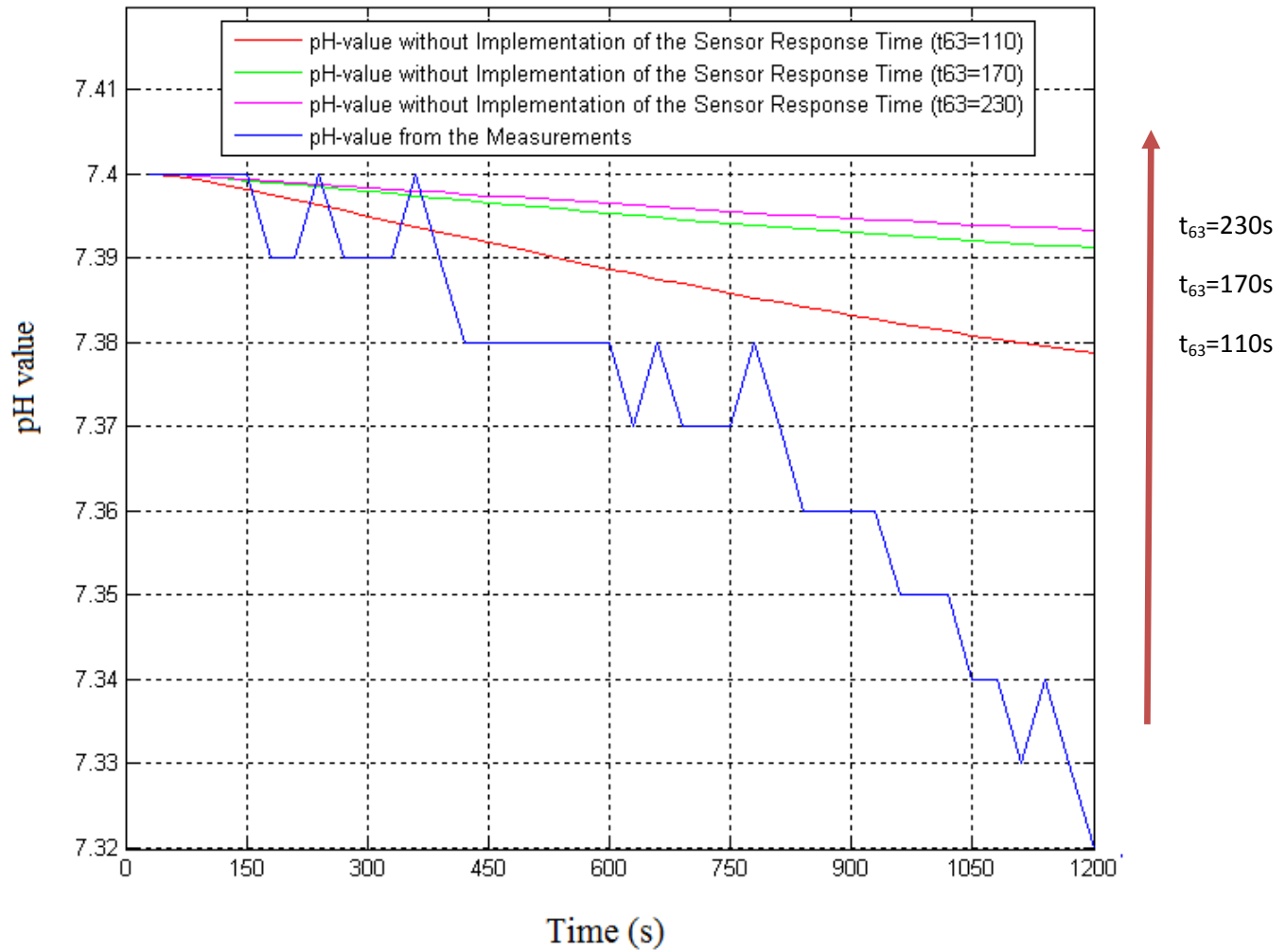


Fig 4.7: The effect of the variation of the pH-sensor response time resulting from the measurement error on the approximation of the measured sensor kinetic for the case of the solution with addition of albumin

From Fig 4.6 and Fig 4.7, it is shown that the lower the response time is, the better is the fit to the measured curves.

From the high correlation coefficients, it can be concluded that the measured curve is a shifted version of the one obtained from the simulation after implementation of the sensor response time. The real response time corresponds then to the lower measured value.

Quantization error

A digital signal is a sequence of samples in which each sample is represented by a finite number of digits. The process of converting a discrete time continuous amplitude signal into a digital signal by expression each sample value as a finite set of discrete values is called quantization error or quantization noise and is given by the relationships:

$$e_q = x_q(n) - x(n) \quad (4.3)$$

$$-\frac{\Delta}{2} \leq e_q(n) \leq \frac{\Delta}{2} \quad (4.4)$$

Where:

- e_q The quantization error
- Δ The quantization step size
- x_q The quantized value of x

In the case of the IMR System, the quantization step is about 0.01, so the quantization error is between -0.005 and 0.005.

The errors occurring during the signal processing of the measured signal (Fig 4.8) are summarized in Tab 4.5.

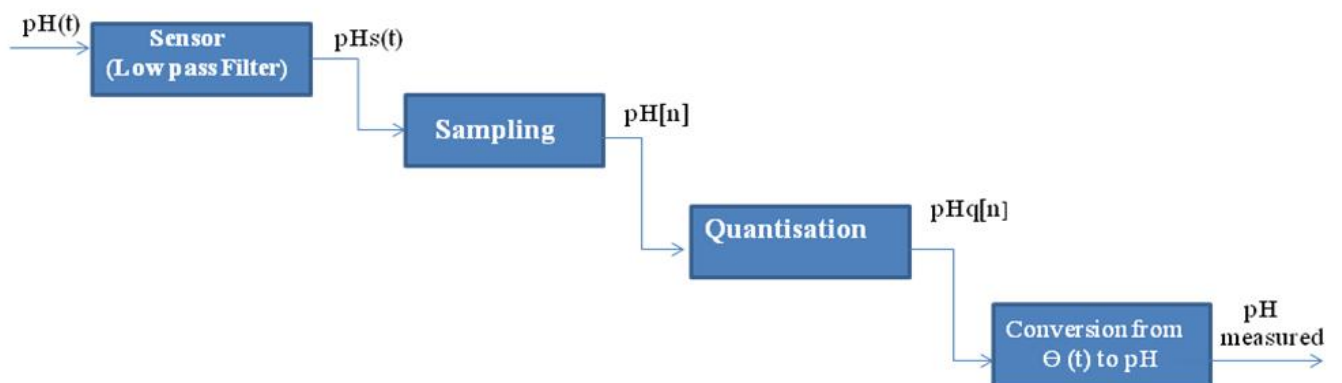


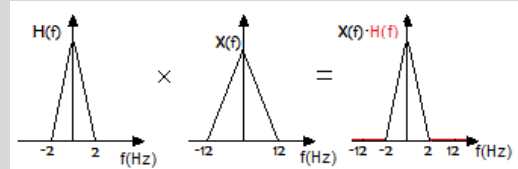
Fig 4.8: The signal flow of the measured pH values

Summary of the signal processing errors

(1)

Effect of the Sensor Impulse Response

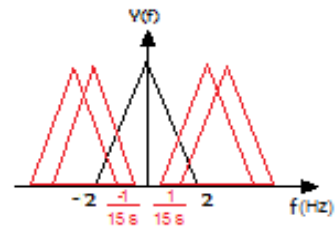
- High Frequencies ($f > 2\text{Hz}$) attenuation
- Amplitude Modulation (with $H(z)$)



(2)

Under Sampling Error (Aliasing)

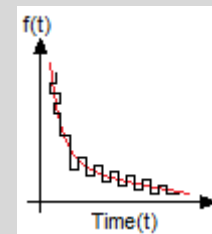
- High Frequencies ($f > 2/30 \text{ Hz}$) attenuation
- Falsification of the measured slope



(3)

Quantization Error

- Falsification of the Amplitude



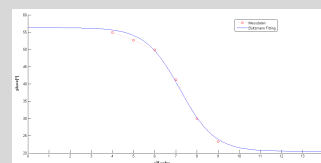
(4)

Noise

(Due to the temperature, convection...)

(5)

Conversion of Φ to a pH value



Tab 4.5 summary of the possible signal processing errors

The simulated Sensor kinetic was convoluted with the sensor response time and then under sampled with a frequency of 0.33 Hz. So, both the impact of the sensor response time and the low sampling frequency resulting errors are taken into account in the simulation (Fig 4.2 and Fig 4.3). The other sources of errors are hard to be modeled.

b. Additional sources of measurement error

Additional errors may be due to actuator electrode performance. This refers to some basic assumptions, i.e. a uniform current density at the anode and the strict fulfillment of Faraday's law (giving the proportionality between the current measured and the generation rate of oxygen and protons).

- In simulation, the interdigitated electrode structure has been simplified to a uniform area. This is reasonable because of the small electrode width and distance (50 μm) which is far below the characteristic dimension of the MRC. However, the assumption of a uniform current density over the whole electrode area was not verified. An experimental verification would require more sophisticated technologies such as electrochemical scanning microscopy, which are currently unavailable.
- Offset currents which are not coupled to anodic water electrolysis: Faraday's law would no longer be valid, if parasitic side reactions contribute to the detected current without evolving oxygen and protons at the stoichiometry described in chapter 2. Two possible side reactions might occur: (1) oxidation of chloride ions and (2) partial oxidation of water with formation of peroxide as a diffusible intermediary product. Reaction (1) has been excluded by the choice of the chloride ion free electrolyte. Reaction (2) has been excluded by an experiment with added catalase enzyme: Catalase rapidly converts peroxide into oxygen and water. If peroxide was produced in relevant amounts, the detected oxygen generation rate should be increased with catalase. However, this was not observed.

4.4.2 Geometry errors

The position of the sensor on the bottom of the MRC varies slightly from well to well. This affects the concentration of both the protons and oxygen molecules detected by the sensor at a determined moment t . A photograph (Fig. 4.9) of the well shows the actual position of the pH sensor which was used to detect the electrolytically generated acid:

DISCUSSION

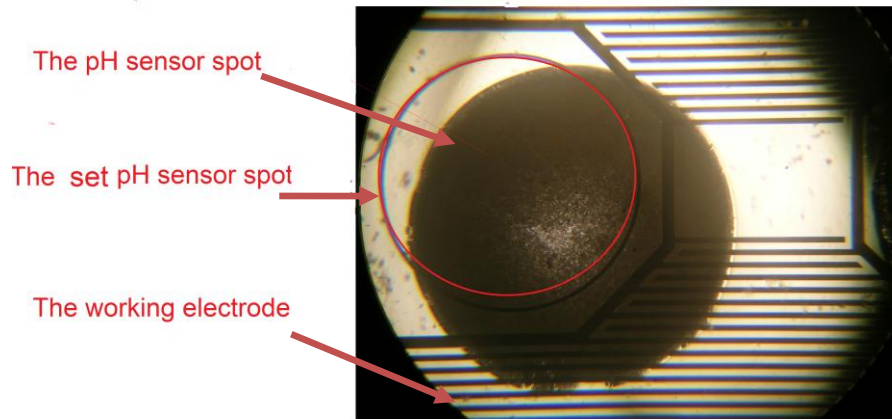


Fig 4.9: a photograph of the pH sensor used for the electrolysis experiment

The ideal sensor position is marked by the circle, the actual sensor has a bigger size (diameter 2.5 mm instead of 2.0 mm) and the position is shifted. Therefore, the part of the electrode covered with the sensor is still electrochemically active. The generated protons and oxygen molecules can diffuse through the sensor.

To examine the influence of the displacement and size of the sensor, the COMSOL model was adjusted for a better approximation of the real geometry, as shown in *Fig 4.11* Fig 4.10.

In order to examine the contribution of the sensor margins and its inside volume to the detected pH values, both a surface and a volume (Fig 4.11) integration over the sensors were carried out.

The obtained pH values after 1200 s simulation time are summarized in Tab 4.6:

	pH value
pH sensor (diameter: 2mm)	5.92
pH sensor (real size and position) surface integration	5.884
pH sensor (real size and position) volume Integration	5.89

Tab 4.6: Comparison between the pH values obtained after 1200 s simulation time

Tab 4.6 shows that the maximum difference between the three pH values obtained from the different simulations is about 0.036 (=5.92-5.884). To investigate the effect of this difference on the approximation of the measured sensor kinetic, we convolute 0.036 with $h(t)$.

DISCUSSION

The convolution can be simplified to a multiplication of 0.36 with $(t-1200)$ with $t=1200$ s (see formula 2.37). A pH decrease of 0.0036 is obtained ($=0.036 \times e^{\frac{-(1200-1200)}{140}} \times \frac{0.14}{140}$).

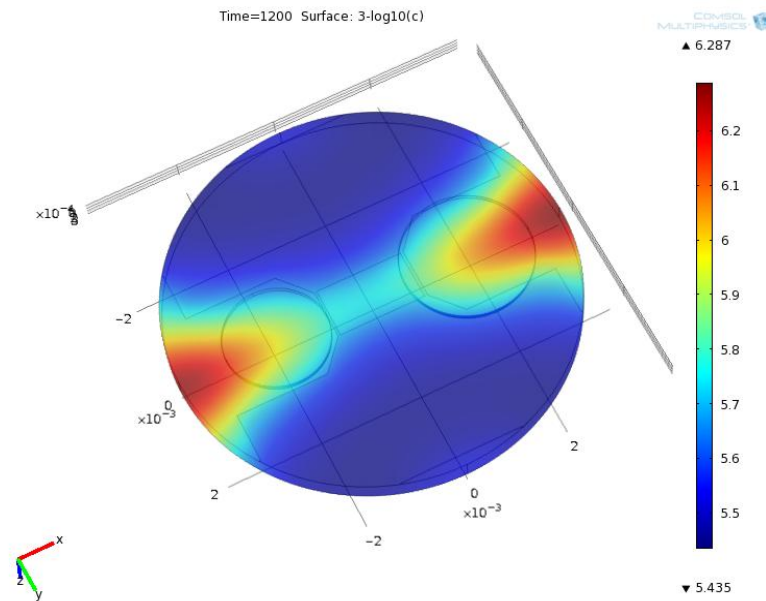


Fig 4.10: The pH distribution in the MRC after adjusting the size and position of the pH sensor

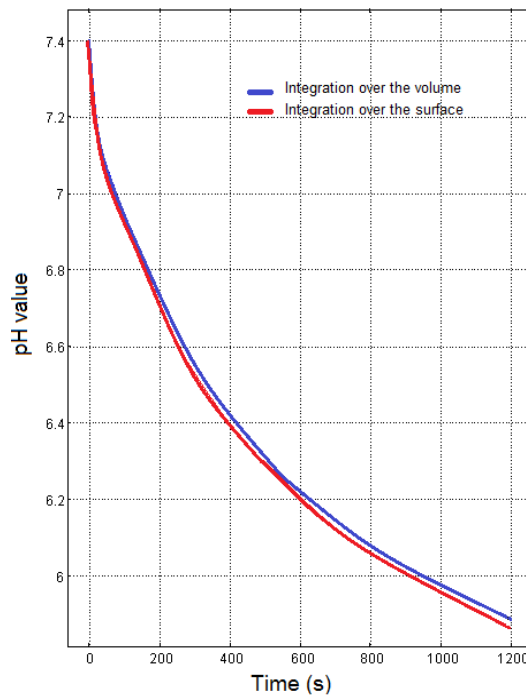


Fig 4.11: Integration over the sensor surface and volume after adjusting the size and position of the pH sensor

4.4.3 Simulation errors

- False assumptions of the Diffusion coefficient D as a function of temperature and buffer capacity. The buffer capacity β again is measured and thus prone to errors.
- Neglecting of material effects (e.g. absorption of O_2 in the polymers confining the MRC)
- Neglecting of mass transport other than diffusion: Convective transport (temperature gradients due to materials and fluids not in thermal equilibrium, local heat production due to electric currents)
- Errors due to discretization: The COMSOL Multiphysics solves the differential equation using a numerical method. Despite being highly sophisticated, time and place discretization errors result. It is assumed however, that this error is small in comparison to the errors discussed above.
- Neglecting of diffusional transport from the side containers: The side containers (pipetting ports) are connected to the MRC by a 1 mm opening filled with electrolyte. The diffusional transport between the side containers and the MRC has been neglected. The distance (center to center) between opening and sensor (pH or O_2) is about 3 mm.

To estimate the error resulting from this neglecting, two simulations with and without the container for both the protons and dissolved oxygen were carried out.

For the case of the pH value a difference of $3 \cdot 10^{-4}$ (pH without container vs. pH with container) is obtained.

As for the dissolved oxygen, the difference lies by 0.5165 % with corresponds to 0.0011 mmol/L.

4.4.4 Quantitative error estimation

With regard to systematic errors (which means biases in measurements that lead to the situation where the mean of many separate measurements differs significantly from the actual value of the measured attribute), one method to approximate the measured error is :

$$dz = \frac{\partial z}{\partial x_1} dx_1 + \frac{\partial z}{\partial x_2} dx_2 + \frac{\partial z}{\partial x_3} dx_3 + \dots = \sum_{i=1}^p \frac{\partial z}{\partial x_i} dx_i \quad (4.5)$$

DISCUSSION

Where z is some function of several (p) variables x . The symbol $\partial z / \partial x_1$ represents the "partial derivative" of the function z with respect to one of the several variables x that affect z .

This approximation is used to estimate the mistake resulting from the calibration and the under-sampling.

The under sampling error (see 4.4.1)

It is hard to estimate the error resulting from the attenuation of the high frequencies, however the effect variance of the response time on the predicted pH value at $t=1200s$ can be approximated as follows:

$$y(t) = h(t) * x(t) \quad (4.8)$$

Where $x(t)$ is the pH value from the simulation, $h(t)$ the impulse response and $y(t)$ the pH value after implementation of the sensor response time

For $t=1200s$, the convolution can be simplified to the multiplication of $x(1200)$ with $h(0)$:

$$y_{1200} = h_{1200} \cdot x(1200) = \frac{\Delta pH}{\tau} \cdot x(1200) \quad (4.9)$$

The derivation of y with respect to τ is:

$$\frac{\partial y}{\partial \tau} = -\frac{\Delta pH}{\tau^2} \cdot x(1200) \quad (4.10)$$

The error Δy resulting from the uncertainty $\Delta \tau$ is :

$$\Delta y = \frac{\partial y}{\partial \tau} \cdot \Delta \tau = -\frac{\Delta pH}{\tau^2} \cdot x(1200) \cdot \Delta \tau \quad (4.11)$$

For a $\Delta \tau = 60s$, the resulting error at $t = 1200s$ is : $\Delta y = \frac{\Delta pH}{\tau} \cdot x(1200) \cdot 60s$

Calculated for $\Delta pH = 0.14$ and $\tau=140$ s the error is about 0.00311.

4.4.5 Summary of the error analysis

Error (at t=1200s) due to...	pH Error +/-	O2 error +/-
<u>Experimental errors</u>		
false calibration	0.05 [12]	$6.42 \cdot 10^{-5}$ [12]
signal drift	≈ 0.005 [12]	$\approx 2.14 \cdot 10^{-5}$ mM [12]
sensor response time	Max 0.05 (Fig 4.6)	≈ 0 mM ($t_{63} \ll 30$ s)
Under-sampling	'not determined'	'not determined'
quantization	0.01 [12]	0.00214mM [12]
unequal current density	'not determined'	'not determined'
electrochemical side reactions	'not determined'	'not determined'
<u>Geometric errors</u>		
sensor position, form and size	0.003	≈ 0 mM
unequal sensor thickness	'not determined'	'not determined'
MRC geometry	'not determined'	'not determined'
<u>Simulation errors</u>		
false values for D	'not determined'	'not determined'
neglecting of material effects	'not determined'	'
neglecting of convective mass transport	'not determined'	'not determined'
neglecting of diffusional transport from the side containers	0.0036	0.0011 mM
Discretization (Comsol, numeric calculation)	'not determined'	'not determined'

Tab 4.7: Quantitative error estimation

The error resulting from the sensor response time is the difference between the pH values with implementation of the sensor response time calculated for the smallest and biggest response time (Fig 4.6).

The errors, that are hard to be quantitatively estimated with the available tools, are flagged with the note 'not determined'.

5 OUTLOOK

Determination of the cell metabolic rate on the basis of the reaction-diffusion model

As stated in the introduction, a valuable application of the validated diffusion and reaction model is the determination of the cell metabolic rate.

The protons released from the cells with a reaction rate R , are transported to the sensor by diffusion. The protons concentration in a specified space-point $\underline{x}(i,j,k)$ in the MRC at a determined moment t is the solution of the second Flick's equation:

$$\frac{dc}{dt} = D \cdot \left(\frac{d^2c}{dx^2} + \frac{d^2c}{dy^2} + \frac{d^2c}{dz^2} \right) + R \quad (5.1)$$

To have a better understanding of the processes affecting the proton's concentration, the solution of the differential equation, $c(t,x,y,z)$, is determined using the finite difference method. This method consists of replacing the derivatives in the differential equation by finite differences:

$$\frac{dc}{dt} = \frac{c_{i,j,k}^t - c_{i,j,k}^{t-1}}{\Delta t} \quad (5.2)$$

$$\frac{dc}{dx} = \frac{c_{i-1,j,k}^t - c_{i,j,k}^t}{\Delta x} \quad (5.3)$$

$$\frac{d^2c}{dx^2} = \frac{c_{i+1}^t - 2 \cdot c_i^t + c_{i-1}^t}{\Delta x^2} \quad (5.4)$$

Where:

$c_{i,j,k}^t$ The proton's concentration in $\underline{x}(i,j,k)$ at t .

$c_{i+1,j,k}^t$ The proton's concentration in $\underline{x}(i+1,j,k)$ at t .

$c_{i-1,j,k}^t$ The proton's concentration in $\underline{x}(i-1,j,k)$ at t .

$c_{i,j+1,k}^t$ The proton's concentration in $\underline{x}(i,j+1,k)$ at t .

$c_{i,j-1,k}^t$ The proton's concentration in $\underline{x}(i,j-1,k)$ at t .

$c_{i,j-1,k-1}^t$ The proton's concentration in $\underline{x}(i,j-1,k-1)$ at t .

$c_{i,j-1,k+1}^t$ The proton's concentration in $\underline{x}(i,j-1,k+1)$ at t .

Δt a finite pace in time

Δx a finite pace in space

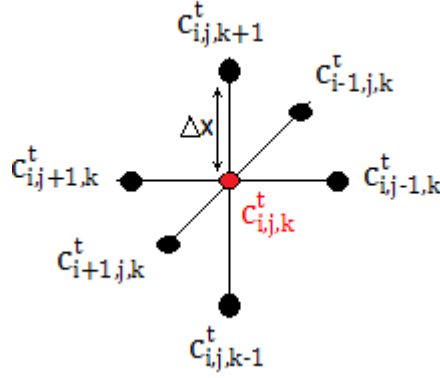


Fig 5.1: The effect of the concentration of the six immediate neighbors of $\underline{x}(i,j,k)$ on its concentration value $c(t,i,j,k)$

By replacing (5.2), (5.3), and (5.4) in (5.1) the following expression is obtained:

$$\frac{c_{i,j,k}^t - c_{i,j,k}^{t-1}}{\Delta t} = R + D \cdot \left(\frac{c_{i+1,j,k}^t - 2 \cdot c_{i,j,k}^t + c_{i-1,j,k}^t}{\Delta x^2} + \frac{c_{i,j+1,k}^t - 2 \cdot c_{i,j,k}^t + c_{i,j-1,k}^t}{\Delta x^2} + \frac{c_{i,j,k+1}^t - 2 \cdot c_{i,j,k}^t + c_{i,j,k-1}^t}{\Delta x^2} \right) \quad (5.4)$$

$$c_{i,j,k}^t = \underbrace{\frac{c_{i,j,k}^{t-1}}{1 + \frac{6 \cdot D}{\Delta x^2}}}_{(1)} + \underbrace{\frac{R}{1 + \frac{6 \cdot D}{\Delta x^2}}}_{(2)} + \underbrace{\frac{D \cdot \frac{\Delta t}{\Delta x^2} (c_{i+1,j,k}^t + c_{i-1,j,k}^t + c_{i,j+1,k}^t + c_{i,j-1,k}^t + c_{i,j,k+1}^t + c_{i,j,k-1}^t)}{1 + 6 \cdot D \cdot \frac{\Delta t}{\Delta x^2}}}_{(3)} \quad (5.5)$$

The Formula (5.5) shows that the $c(t,i,j,k)$ depends on three processes:

- (1) Its previous value $c_{i,j,k}^{t-1}$
- (2) The reaction rate R
- (3) The concentration of its six neighboring points apart from $\underline{x}(i,j,k)$ in the three space dimensions (diffusion process)

From (5.4) we can conclude that the reaction rate can't be obtained by the simple time derivation of $c(t,i,j,k)$. The time derivation of $c(t,i,j,k)$ is in fact the superposition of the reaction rate and the diffusion process (presented here by the effect of the six neighboring space points).

Besides, the detected concentrations don't correspond to the real ones (which are the solutions of the Fick's diffusion equation), as they are modified by the sensor impulse response, the low sampling rate and the quantization effect.

A quite good approximation of the reaction rate can be obtained with means of the developed COMSOL Model.

First, it can be assumed that the reaction rate is a constant. The main steps are: Variation of the rate value in the model, convolution of the simulated sensor kinetics with different sensor impulse responses (with different response times from the variance range) and sampling the resulting curves with a frequency of 0.033 Hz. The obtained curves are then compared to the ones obtained from the measurements.

If a difference between the slopes emerges, it can be concluded that the reaction rate isn't a constant. Variable reaction rates of cells (within a single measurement period of ≈ 1200 s) may occur as a metabolic response to micro environmental conditions of pH and dissolved oxygen which are altered during the rest interval of each measurement period. An altered rate can be approximated by introducing different functions ($\approx \exp(-at)$, $\approx a/t$).

It is evident however, that the different parameters that may be varied to achieve a "good" congruence between measured and simulated curve also impose a danger of misinterpretation of experimental data.

As shown in the error analysis section, the current data analysis of the IMR system is erroneous in different ways. It can be improved by, using pH sensors with lower response time and then increasing of the sampling rate. In fact increasing the sampling rate with conservation of the current sensors is unlikely to lead to better results. This is due to the low pass characteristic of the sensor. Thus, the high frequencies of the signal, corresponding to the high slopes in time domain, are attenuated before the sampling. The under-sampling of the sensor's measured signal causes a further loss of the remaining high frequencies because of the aliasing effect.

Once sensors with lower response time are used and a sampling rate obeying the Nyquist sampling theorem is set, the real pH sensor kinetic can be reconstructed from the measured one by integration of a real time system in the IMR System, which compensates the effect of the sensor response time by transforming the obtained values in frequency domain and then multiplying them with $1/H(z)$.

The use of the pH sensor with a shorter response time is particularly recommended for another validation experiment to eliminate the remaining uncertainty about the model.

6 SUMMARY

In the present thesis, a previously developed reaction-diffusion model for ex-vivo microphysiometry was extended by the consideration of aspects from measurement engineering and signal analysis. In particular, the response time of pH and dissolved oxygen sensors were implemented into the model to provide a basis for a direct comparison of simulated sensor kinetics with experimental kinetics. This again is a precondition for a validation of the model which is necessary to show that no relevant physico-chemical processes have been neglected. For model validation, a novel electrochemical approach was pursued to have the reaction rate under control by measuring the current coupled to anodic water electrolysis. The validation yielded a good agreement of experiment and simulation with correlation coefficients ranging between 0.95 and 0.97.

7 LIST OF FIGURES

Fig 1.1: Flow of the verification and validation process. Validation is used to quantify the model's ability to describe the experimental outcomes of the physical system, given well defined boundary settings and initial conditions.....	8
Fig. 2.1: IMR system with embedded process microscope and pipetting robot in a cell culture incubator. The sensor test plate is in front position.....	10
Fig 2.2: (A) The sensor test plate with its cover lid, confining 24 micro reaction volumes on each of the cell culture wells. The bottom of the plate is a glass substrate. (B) Enlargement of a single well in top view, with optochemical acidification sensor (AS), optochemical oxygen sensor (OS) and interdigitated electrode structure (IE).....	11
Fig 2.3: Pipetting system showing a MRC in cross section together with two hydrostatic side vessels.....	12
Fig 2.4 : VoltaLab potentiostat.....	12
Fig 2.5: (a) Idealized Geometry of the MRC (at the top: top view, below: section), (b) Layout of the MRC with the electrode dimensions, (c) Two Dimensional geometry of the MRC in COMSOL representation,(d) Three Dimensional geometry of the MRC in COMSOL representation.	13
Fig. 2.6: Set up and flow of the electrolysis.....	17
Fig 2.7: The reduction and oxidation reactions occurring during the electrolysis experiment	17
Fig 2.8: (a) Cyclic Voltammetry waveform (b) Typical cyclic voltogrammm	19
Fig 2.9: The Chronoamperometry set up with the VoltaLab	22
Fig 2.11: Components of the output signal in the chronoamperometry.....	23
Fig 2.12: the electrode double layer's equivalent electrical circuit.....	23
Fig 2.13: The distribution of ions at the metal/solution interface [5]	24
Fig 2.14: The Z Plot Software Interface showing the Impedance Spectroscopy parameters...	25
Fig 2.15: The Nyquist Plot of the MRC System circuit model.The red curve is the measured curve, the green one is the fitting curve.	26
Fig 2.16: The equivalent circuit of the MRC given by the Z-Plot program.....	26
Fig 2.17: Implementation of the measured current as an interpolated function in COMSOL.	30
Fig 2.18: Titration curve of the medium without addition of albumin	31
Fig 2.19: Titration curve of the medium with addition of albumin.....	31

LIST OF FIGURES

Fig 2.20: Schematic of the single exponential decay ($t_0 > t_1$).....	35
Fig 2.21: The fluorophore is excited with a sinusoidally modulated light. Emission is delayed in phase expressed by the phase angle Φ relatively to the excitation signal, caused by the decay time of the excited state	35
Fig 2.22: Relationship between the measured pH and the phase angle	36
Fig 2.23: Discrepancy between the ideal curves (in black) and the measured ones (in red). The left Graph is a sketch showing the sensor response to a step of pH. The right graph is the response to a step of pH (resulting, e.g. from an instantaneous medium exchange in the test plate) followed by a linear pH decrease caused by the cell metabolic activity (according e.g. to a constant cell metabolic rate).....	38
Fig 2.24: Relationship between the time domain and the frequency domain for LTI Systems	39
Fig 2.25: Step response of the oxygen Sensor showing a very short response time of ≈ 15 s..	41
Fig 2.26: The pH sensor step responses for the case of the solution with and without albumin.....	41
Fig 2.27: Impulse response of the pH Sensor for the case of (a) a solution with addition of albumin, (b) a solution without addition of albumin.....	42
Fig 3.1: The measured dissolved oxygen given in % saturation and in concentration during an electrolysis experiment (Electrolysis start at $t=360$ s)	45
Fig 3.2: The measured pH curves during the electrolysis experiment for the case of a buffer solution with and without addition of albumin (Electrolysis start at $t=330$ s).....	45
Fig 3.3: The dissolved oxygen distribution in a closed MRC 1200 s after start of the electrolysis.....	47
Fig 3.4: The calculated kinetic of dissolved oxygen sensor during 1200 of oxygen generation in the closed MRC.....	47
Fig 3.5: The pH value distribution in a closed MRC after 1200 s of start of the electrolysis for the case of the solution without addition of albumin	48
Fig 3.6: The calculated kinetic of the pH sensor during the 1200 s of the electrolysis reaction in the closed MRC for the case of the buffer solution without addition of albumin.....	49
Fig 3.7: The dissolved oxygen distribution in a closed MRC 1200 s after start of the electrolysis for the case of the solution with addition of albumin	49
Fig 3.8: The calculated kinetic of the pH sensor during the 1200 s of the electrolysis reaction in the closed MRC for the case of the buffer solution with addition of albumin.....	50

LIST OF FIGURES

Fig 3.9: Kinetic of the pH Sensor between 0 and 1200 s with consideration of the sensor response time for the case of a buffer solution without addition of albumin and a sensor response time of 140 s. 50

Fig 3.10: Kinetic of the pH Sensor between 0 and 1200 s with consideration of the sensor response time, for the case of a buffer solution with addition of albumin and a sensor response time of 270 s. 51

Fig 3.11: (a) Frequency response of the pH-sensor $H(z)$; (b) the Fourier Transformed of the sensor kinetic resulting from the simulation $X(z)$; (c) The convolution result of $x(t)$ and $h(t)$ 52

Fig 4.1: Comparison between the measured dissolved oxygen sensor kinetic and the simulated one 54

Fig 4.2: Comparison between the simulated sensor kinetic, the measured one and the one obtained after the implementation of the sensor response time for the case of the buffer solution without addition of albumin 55

Fig 4.3: Comparison between the simulated sensor kinetic, the measured one and the one obtained after the implementation of the Sensor Response Time for the case of the buffer solution with addition of Albumin 56

Fig 4.4: The real oxygen rate (in green) and the measured one (in red). The maximum error resulting from the low sampling rate is 30s (At the beginning of the measurement) 60

Fig 4.5: The real pH value (in red) and the measured one (in green).The maximum error $\Delta\tau$ resulting from the low sampling rate is ± 60 s (30 s at the beginning and 30 s at the end of the measurement) 60

Fig 4.6: The effect of the variation of the pH-sensor response time resulting from the measurement error on the approximation of the measured sensor kinetic for the case of the solution without addition of albumin 61

Fig 4.7: The effect of the variation of the pH-sensor response time resulting from the measurement error on the approximation of the measured sensor kinetic for the case of the solution with addition of albumin 62

Fig 4.8: The signal flow of the measured pH values..... 63

Fig 4.9: a photograph of the pH sensor used for the electrolysis experiment 66

Fig 4.10: The pH distribution in the MRC after adjusting the size and position of the pH sensor..... 67

Fig 4.11: Integration over the sensor surface and volume after adjusting the size and position of the pH sensor..... 67

Fig 5.1: The effect of the concentration of the six immediate neighbors of $x(i,j,k)$ on its concentration value $c(t,i,j,k)$ 72

8 LIST OF TABLES

Tab 2.1: The Impedance spectroscopy results	27
Tab 2.2: The capacitive current decay constant for both the solution with and without albumin.....	28
Tab 2.3: Experimental determination of the buffering capacity in the medium without addition of albumin	31
Tab 2.4: Experimental determination of buffer capacity in the culture medium with addition of albumin	31
Tab 2.5: Diffusion coefficients in water.....	34
Tab 4.1: Comparison of the results (simulated and measured) of the dissolved oxygen.....	54
Tab 4.2: Comparison of the results (simulated, measured and obtained after the implementation of the sensor response time).....	55
Tab 4.3: Comparison of the results (simulated, measured and obtained after the implementation of the sensor response time) for the case of the buffer solution with addition of Albumin.	56
Tab 4.4: The influence of the working electrode variation on the final value of the dissolved oxygen concentration.	58
Tab 4.5: Summary of the possible signal processing errors.....	64
Tab 4.6: Comparison between the pH values obtained after 1200 s simulation time.....	66
Tab 4.7: Quantitative error estimation	70

9 REFERENCES

Publications:

1. A. M. Otto, B. Booß-Bavnbek et al. (eds.): Cell Cultivation and Sensor-Based Assays for Dynamic Measurements of Cell Vitality, BetaSys, Systems Biology 2, 221; DOI 10.1007/978-1-4419-6956-9_10, C Springer Science+Business Media, LLC 2011
2. Brischwein, M., Grundl, D., Zhang, X., Wolf, B. Finite-Element Modelling of Microphysiometry on Cellular Specimen, World Congress on Medical Physics and Biomedical Engineering, September 7. – 12. 2009, Munich, Germany, ISBN 978-3-642-03472-5, S. 30-33 , IFMBE Proceedings, Volume 25/VII, Olaf Dössel and Wolfgang C. Schlegel, Springer Heidelberg, 2009
3. W. Junge and S. McLaughlin: The role of fixed and mobile buffers in the kinetic of proton movement“. Biochim. Biophys Acta, 1987, 890, 1-5
4. H B Henninger, S P Reese, A E Anderson, and J A Weiss: Validation of computational models in biomechanics. Proceedings of the Institution of Mechanical Engineers, Part H: Journal of Engineering in Medicine, 2010, 224, 801-812; DOI: 10.1243/09544119JEIM649 <http://pih.sagepub.com/content/224/7/801.full.pdf+html>
5. T. Geisler, J. Ressler, H. Harz, B. Wolf, R. Uhl. Automated Multiparametric Platform for High-Content and High-Throughput Analytical Screening on Living Cells. *IEEE Transactions on automation science and engineering*, Vol. 3, No. 2, April 2006, 169-176

Books:

6. Carl H.Hamann, Wolf Vielstich: Electrochemie. Fourth Edition, Wiley-VCH Verlag GmbH & Co KGaA, 2005, Weinheim.
7. John G. Proaskis, Dimitris G.Manolakis: Digital Signal processing Principles, Algorithms, and Applications. Fourth Edition, Upper Saddle River, 2007, New Jersey.
8. E.Schruefer: Elektrische Messtechnik. Third Edition, Carl Hanser Verlag München Wien, 1988, Würzburg.

Theses and Reports:

9. X. Zhang, Finite Elemente Modellierung zur Sensor-Detektion von zellmetabolischer Aktivität. Bachelor Thesis at Technische Universität München, Heinz Nixdorf-Lehrstuhl für Medizinische Elektronik (2009)

10. X. Zhang, Finite Elemente Modellierung von Diffusion, Reaktion und Strömung in Mikrovolumina im Hinblick auf Zellmetabolismus. Diploma Thesis at Technische Universität München, Heinz Nixdorf-Lehrstuhl für Medizinische Elektronik (2010)

11. Safa Messaoud: Experimental examination of the effect of long sensor response times. Project Work at Universität München, Heinz Nixdorf-Lehrstuhl für Medizinische Elektronik (2010)

Others:

12. Instruction Manual pH-1 mini, PreSens Regensburg, Germany